



Insights into nitrogen and boron-co-doped graphene toward high-performance peroxyomonosulfate activation: Maneuverable N-B bonding configurations and oxidation pathways



Xiao Chen^{a,b}, Xiaoguang Duan^c, Wen-Da Oh^d, Peng-Hui Zhang^e, Chao-Ting Guan^f, Yi-An Zhu^g, Teik-Thye Lim^{a,b,*}

^a Environmental Chemistry and Materials Centre, Nanyang Environment and Water Research Institute (NEWRI), Nanyang Technological University (NTU), 1 Cleantech Loop, CleanTech One, #06-08, 637141, Singapore

^b School of Civil and Environmental Engineering, Nanyang Technological University, 50 Nanyang Avenue, 639798, Singapore

^c School of Chemical Engineering, The University of Adelaide, Adelaide, SA 5005, Australia

^d School of Chemical Sciences, Universiti Sains Malaysia, 11800 Penang, Malaysia

^e School of Chemical and Biomedical Engineering, Nanyang Technological University, 62 Nanyang Drive, 637459, Singapore

^f State Key Laboratory of Urban Water Resource and Environment, Harbin Institute of Technology, Harbin 1500090, China

^g State Key Laboratory of Chemical Engineering, East China University of Science and Technology (ECUST), Shanghai 200237, China

ARTICLE INFO

Keywords:

Nitrogen and boron-co-doped graphene

Radical pathway

Non-radical pathway

Peroxyomonosulfate

Density functional theory

ABSTRACT

Nitrogen and boron-co-doped graphene was synthesized through two-step thermal annealing (2sNBG) which was employed as a PMS activator to degrade sulfacetamide (SAM). The concentration of the main reactive functionalities (pyridinic N and substitutional B (BC3)) as well as catalytic activity of 2sNBGs were delicately maneuvered through tuning the thermal annealing temperatures. The catalytic performances of the doped graphene in this study followed the order of 2sNBG800 > 2sNBG900 > 2sNBG700 > 2sNBG600 > NG600 > 1sNBGs > BG800. 30.4 at.% N of h-BN ($N_{h\text{-}BN}/N_{\text{total}}$) and 32.8 at.% B of h-BN ($B_{h\text{-}BN}/B_{\text{total}}$) were detected in the 1sNBG800, which hampered the catalytic oxidation of SAM via PMS activation by 1sNBG. Among all the 2sNBGs, 2sNBG800 (2sNBG prepared at 800 °C) possessed the highest level of N (13.8 at.%) and B (16.3 at.%), the highest content of pyridinic N (73.4 at.%, $N_{\text{pyridinic-N}}/N_{\text{total}}$) and BC3 (43.4 at.%, $B_{\text{BC3}}/B_{\text{total}}$), the lowest B-C-O (56.6 at.% BC2O, $B_{\text{BC2O}}/B_{\text{total}}$) content and none of h-BN. 2sNBG800 performed best to activate PMS for catalytic oxidation of SAM. Both radical quenching experiment and DFT calculation revealed that the introduction of B into NG can facilitate the transition from a non-radical oxidation dominating in the NG/PMS system to the coexistence of non-radical and radical oxidation in the 2sNBG/PMS system. The synergistic coupling effect between pyridinic N and BC3 (bonding configuration of B-C-C-pyridinic N) was the main reason for the enhanced catalytic activity of 2sNBG800. The transformation of the amine group and subsequent mineralization can effectively minimize the hazardous potentials of sulfonamides to the environment. The SAM degradation was negligibly influenced by NO_3^- in the 2sNBG800/PMS/SAM system, while Cl^- and humic acid led to 33% and 64% decrease in k_{app} , respectively. The adsorbed intermediates mainly accounted for the deactivation of 2sNBG. This study provides an insight into the function of different N-B bonding configurations in NBG for metal-free catalytic oxidation.

1. Introduction

Catalytic oxidation via reactive oxygen species (ROS) produced from peroxyomonosulfate (PMS) activation has proved to be effective for decomposition of toxic and recalcitrant organic contaminants in the aqueous environment [1,2]. Compared with the tradition metal-based

catalysts (e.g., Co(II)/cobalt oxides, Mn(II)/manganese oxides, Fe(II)/iron oxide, etc.) for PMS activation, carbocatalysts have emerged as the metal-free, environmentally friendly and biocompatible alternatives to activate PMS during the past few years [3,4]. Carbocatalysts can overcome the problematic toxic metal leaching and secondary contamination in metal-based catalysis [5,6].

* Corresponding author at: Environmental Chemistry and Materials Centre, Nanyang Environment and Water Research Institute (NEWRI), Nanyang Technological University (NTU), 1 Cleantech Loop, CleanTech One, #06-08, 637141, Singapore.

E-mail address: CTTLIM@ntu.edu.sg (T.-T. Lim).

Among diverse nanocarbon allotropes, the two-dimensional (2D) graphene has garnered significant research interest due to its high theoretical specific surface area (SSA, $2630\text{ m}^2\text{ g}^{-1}$) as well as its fascinating electronic, thermal and mechanical properties [7]. However, pristine graphene with intact sp^2 hybridized hexagonal lattice demonstrates catalytic inertness due to its limited surface functionalities, zero band gap and low chemical potentials [8,9]. Heteroatom doping (e.g., nitrogen, boron, sulfur or phosphorus) as a chemical modification technique can promote the catalytic capability of graphene by tailoring its surface properties, breaking the electroneutrality of sp^2 hybridized nanocarbon framework and creating more charged active sites [10].

Nitrogen-doped graphene (NG) employed to activate PMS for the removal of aqueous organic pollutants has been most researched and it exhibits excellent catalytic performance [3,10,11]. N bonding configuration can be effectively tuned by adjusting the synthesis temperature [12]. The reported possible mechanisms include radical pathway involving sulfate radical ($\text{SO}_4^{\cdot-}$) and hydroxyl radical (HO^{\cdot}) [13] and non-radical pathway involving surface activated species [14], surface-bound $\text{SO}_4^{\cdot-}$ [15,16] and singlet oxygen (${}^1\text{O}_2$) [17]. In contrast, it has been reported that boron-doped graphene (BG), phosphorus-doped graphene (PG) or sulfur-doped graphene (SG) exhibit limited catalytic activity toward PMS activation for phenol degradation [18,19]. Hence, it comes naturally to a question whether co-doping could further improve the catalytic performance of carbocatalyst as PMS activator. Co-doping with phosphorus or iodine is not effective in enhancing the catalytic activity of NG for phenol degradation via PMS activation at the current state of knowledge [20]. However, sulfur and nitrogen co-doped graphene exhibited a remarkably enhanced catalytic performance to activate PMS for degradation of phenol and bisphenol A [19,21].

N and B atoms are promising candidates for co-doping graphene, which can be explained by 1) similar atomic radii between C (0.77 Å), N (0.70 Å) and B (0.82 Å) keep the total number of electrons in the sp^2 hybridized graphitic sheets of nitrogen and boron-co-doped graphene (NBG) unchanged; and 2) the synergistic coupling effects can be induced by the coexistence of N (electron-rich) and B (electron-deficient) atoms (electronegativity (χ): χ_{N} (3.04) > χ_{C} (2.55) > χ_{B} (2.04)) [22]. The bonding configuration of N and B atoms in the graphitic framework of NBG is a pivotal factor affecting the catalytic activity of NBG. The B-C-N heteroring (especially B atom is meta to N atom) in the NBG fabricated by a two-step synthesis method has been reported to exhibit synergistic effect that renders NBG a superior electrocatalyst over NG or BG [23]. On the other hand, hexagonal boron nitride (h-BN) has been reported to form during the one-step NBG synthesis, which exhibited chemical inertness and hampered oxygen reduction reaction (ORR) catalyzed by NBG [24,25]. However, h-BN has also been claimed to play a key role in nitroarenes reduction catalyzed by NBG [26] and serve as adsorbent for organic contaminants [27,28]. Thus, the formation of N-B bonding configuration is closely associated with synthesis method and it remains disputable in terms of the catalytic activity of different N-B bonding configurations toward PMS activation.

So far, most research about NBG as carbocatalyst is related to ORR [23–25,29], triiodide reduction [30], and nitroarenes reduction [26]. To the best of our knowledge, limited research has focused on NBG acting as a carbocatalyst to activate PMS for degradation of aqueous organic contaminants. Sun et al. [20] claimed that NBG (0.1 wt% B_2O_3) prepared by one-step thermal annealing (GO + ammonium nitrate + ammonium pentaborate octahydrate) outperformed NG as PMS activator to degrade phenol, whereas Duan et al. [18] reported the reverse scenario and proposed the formation of h-BN as a reason for the deteriorated catalysis. Thus, it is still debatable in terms of the catalytic activity of NBG for PMS activation to degrade the aqueous organic contaminants. Besides, the reactive N-B bonding configurations in carbocatalysis need to be identified.

Herein, in this study, the hypotheses are proposed as follows: 1) NBG dominated by h-BN or B-C-N heteroring can be realized by

deliberately designed synthesis methods (thermal annealing with common C (GO), N (urea) and B (H_3BO_3) precursors under different sequences: one step or two steps); 2) the concentration of different N-B bonding configurations can be tuned by adjusting the synthesis conditions (e.g., synthesis temperature); and 3) NBG with different N-B bonding configurations will demonstrate different catalytic activities to activate PMS for degradation of aqueous organic contaminants in terms of degradation kinetics, catalytic mechanism and reusability.

Thus, the objectives of this study are as follows: 1) to synthesize two-step NBG (2sNBG) free of h-BN via the deliberately designed two-step thermal annealing, whereby NG was first synthesized via thermal annealing, followed by incorporation of B atoms via second-step thermal annealing; 2) to synthesize one-step NBG (1sNBG) containing h-BN via the deliberately designed one-step thermal annealing, whereby the mixture of GO, urea and H_3BO_3 was calcined in one-pot mode; 3) to fabricate 2sNBGs possessing different doping levels of N and B atoms as well as N-B bonding configurations through tuning the thermal annealing temperature (T_a) (600, 700, 800 and 900 °C); 4) to investigate the effect of T_a on the structural and compositional properties (e.g., SSA, doping levels of N and B atoms, N-B bonding configuration, etc.) of 2sNBGs; 5) to explore catalytic capabilities of 2sNBGs via PMS activation for degradation of toxic and recalcitrant organic contaminants in the aqueous environment, the catalytic mechanism of PMS activation, degradation pathway and reusability; and 6) to fabricate 1sNBGs under selected T_a (600, 700, 800 and 900 °C) and compare the compositional and structural properties as well as catalytic performances between 1sNBG and 2sNBG. Sulfonamide antibiotics (their widespread distribution in water possibly induces evolution of antibiotic-resistant bacteria) [31,32] have been proven to be effectively degraded by various PMS activation processes (e.g., Co-doped $\text{g-C}_3\text{N}_4$ /PMS/sulfathiazole (STZ) [33] and Co/Fe oxide/PMS/sulfamethoxazole (SMX) [34]). However, to date, the investigation with sulfacetamide (SAM) as the target pollutant for PMS activation processes via carbocatalyst is limited. It has been reported that SAM can be effectively degraded in NG/PMS/SAM system [12]. Hence, SAM was selected in this study to investigate the catalytic activity of NBG via PMS activation.

2. Experimental

2.1. Chemicals

The chemicals employed in this study include graphite powder (> 99.9%, Alfa Aesar), hydrogen peroxide (30%, Alfa Aesar), concentrated sulfuric acid (98%, Sigma-Aldrich), potassium permanganate (99%, Sigma-Aldrich), sodium nitrate (99%, Sigma-Aldrich), hydrochloric acid (37%, Sigma-Aldrich), peroxymonosulfate (commercially available as Oxone (2 $\text{KHSO}_5\text{KHSO}_4\text{K}_2\text{SO}_4$), Alfa Aesar), urea (99.0–100.5%, Sigma-Aldrich), boric acid (> 99%, Sigma-Aldrich), SAM (≥ 98%, Sigma-Aldrich), sulfanilamide (SNM) (≥ 98%, Sigma-Aldrich), SMX (≥ 98%, Sigma-Aldrich), STZ (≥ 98%, Sigma-Aldrich), nitrobenzene (NB) (≥ 99%, Sigma-Aldrich), humic acid (technical grade, Merck), absolute ethanol (≥ 99.5%, Merck), methanol (≥ 99.9%, Sigma-Aldrich), sodium hydroxide (≥ 98%, Sigma-Aldrich), sodium chloride (≥ 99.5%, Alfa Aesar). All the chemicals were used without further purification. Milli-Q ultrapure water with a resistivity of 18.2 MΩ cm (25 °C) was used for all the experiments.

2.2. Two-step synthesis

Step 1: NG600 synthesis

The modified Hummers' method was employed to synthesize graphene oxide (GO) [35] (Text S1). In a typical run, GO (200 mg) was dissolved in 100 mL water and sonicated for 30 min. Then urea (1 g) was added into the GO solution and magnetically stirred for 30 min (500 rpm), followed by heating the mixture to 55 °C (magnetically

stirred, 500 rpm) for water evaporation. After grinding, the dried mixture was transferred to a quartz boat and then into the tubular furnace for calcination (600 °C, N₂, 30 min, ramping rate = 5 °C min⁻¹). Afterwards, the product was ground, filtered and washed several times with absolute ethanol and water, and then dried in an oven at 60 °C. The final product was designated as NG600. NG800 was prepared following the similar procedure except for calcination at 800 °C.

Step 2: 2sNBG synthesis

Exactly 100 mg NG600 was put into 50 mL water and sonicated for 30 min. Then 500 mg H₃BO₃ was added into the NG600 suspension and sonicated for another 30 min for H₃BO₃ dissolution. The mixture was then heated to 55 °C (magnetically stirred, 500 rpm) for water evaporation. After grinding, the dried NG600/H₃BO₃ mixture was transferred to a quartz boat and then into the tubular furnace operated under N₂ atmosphere. The furnace was progressively heated at a ramping rate of 10 °C min⁻¹ to the desired T_a (600, 700, 800 and 900 °C) and maintained for 30 min. The products were then ground and put into the 80 °C Milli-Q ultrapure water (magnetically stirred, 500 rpm) to dissolve the impurities (such as the residual B₂O₃). Afterwards, the products were filtered and washed several times with absolute ethanol and water, and then dried in an oven at 60 °C. The final products prepared via the two-step approach were designated as 2sNBG600, 2sNBG700, 2sNBG800 and 2sNBG900, respectively.

2.3. One-step synthesis

For comparison, NBG was also synthesized via one-step thermal annealing method. GO (200 mg) was dissolved in 100 mL water and sonicated for 30 min. Then 1 g urea and 500 mg H₃BO₃ were added and sonicated for another 30 min for dissolution of urea and H₃BO₃. Then the mixture was heated to 55 °C (magnetically stirred, 500 rpm) for water evaporation. After grinding, the dried GO/urea/H₃BO₃ mixture was transferred to a quartz boat and then into the tubular furnace operated under N₂ atmosphere. The furnace was progressively heated at a ramping rate of 10 °C min⁻¹ to the desired T_a (600, 700, 800 and 900 °C) and maintained for 30 min. The products were then ground and put into the 80 °C Milli-Q ultrapure water (magnetically stirred, 500 rpm) to dissolve impurities (such as the residual B₂O₃). Afterwards, the products were filtered and washed several times with absolute ethanol and water, and then dried in an oven at 60 °C. The final products prepared via the one-step approach were denoted as 1sNBG600, 1sNBG700, 1sNBG800 and 1sNBG900, respectively. The synthesis procedure for reduced graphene oxide (rGO800) and BG800 can be found in **Text S1**.

2.4. Characterization

The crystallographic structure of carbocatalysts was studied through X-ray diffraction (XRD, Bruker AXS D8 Advance) equipped with high-intensity monochromatic Cu-Kα (40 kV, 40 mA, $\lambda = 1.5418 \text{ \AA}$) at a scan rate of 0.02 ° s⁻¹ with a 2θ range of 5–80°. Field emission scanning electron microscopy (FESEM, JEOL JSM-7600 F) and transmission electron microscopy (TEM, JEOL JEM-2010) were used to analyze the morphology and structure of carbocatalysts. Elemental mapping was acquired on an Energy-dispersive X-ray (EDX) spectrometer (Oxford Xmax80 LN₂ Free) connected with FESEM. The thermogravimetric analyzer (PerkinElmer, TGA-4000) was used to investigate the thermal stability of carbocatalysts (ramping rate = 10 °C min⁻¹, air). N₂ adsorption-desorption isotherm acquired on Quantachrome Autosorb-1 analyzer (77 K) was employed to probe the SSA and pore size distribution. The PerkinElmer GX Fourier transform infra-red (FTIR) system was used to explore the surface functionalities on carbocatalysts. The Kratos Axis Supra spectrophotometer with a dual anode monochromatic K α excitation source was employed for X-ray photoelectron spectroscopy (XPS) analysis. An adventitious carbon C1s core level

(284.8 eV) was used to correct the binding energies of C, O, N and B elements. The deconvolution of all XPS peaks was carried out on CasaXPS software using Gaussian-Lorentzian function in the Shirley background. The LabRAM ARAMIS Horiba Jobin Yvon instrument was used to record Raman spectra (532 nm).

2.5. Evaluation of SAM catalytic oxidation

The performance of NBG was evaluated as PMS activator to degrade aqueous SAM. A 50-mL solution containing 10 mg L⁻¹ SAM and 0.5 mM PMS was prepared in a 100-mL beaker, followed by the addition of carbocatalyst (0.2 g L⁻¹) into the solution (pH_{initial} = 7). The suspension was magnetically stirred at 600 rpm to initiate the catalytic oxidation. Solution sample (0.5 mL) was taken and filtered (0.45 μm hydrophilic polyethersulfone membrane) at designated time intervals, and then immediately quenched with 0.5 mL methanol. Then the SAM concentration in the filter solution was determined by high-performance liquid chromatography (HPLC, PerkinElmer) with a Hypersil gold C18 reverse phase column (150 mm × 4.6 mm × 5 μm) and UV detector set at $\lambda_{\text{max}} = 256 \text{ nm}$. The mobile phase was a mixture of methanol and water (6:4). The flow rate was set at 0.6 mL min⁻¹. The adsorption experiment was similar to the catalytic experiment except the addition of PMS and methanol as quenching agent.

The effect of catalyst loading (0.1, 0.2 and 0.3 g L⁻¹), PMS dosage (0.2, 0.5 and 0.9 mM), and common matrix species ([Cl⁻] = 100 mg L⁻¹, [NO₃⁻] = 10 mg L⁻¹, [humic acid] = 5 mg L⁻¹) on the SAM removal in the 2sNBG/PMS/SAM system was probed. The possible ROS in the 2sNBG/PMS/SAM system was explored using ethanol and NB as radical scavengers. The main transformation products of SAM generated in the 2sNBG/PMS/SAM system were probed via LC-MS/MS (6460C Triple Quadrupole LC/MS, Agilent). The mobile phase was methanol (0.1% formic acid) and water (0.1% formic acid). Shimadzu TOC-vcpb analyzer was used to analyze total organic carbon (TOC). Each of the experiments was carried out in triplicate. The results were reported as the average of three runs. The ecotoxicity of SAM and its transformation products (TPs) was estimated by Quantitative structure-activity relationship (QSAR) analysis via Ecological Structure-Activity Relationship Model (ECOSAR) program.

2.6. Reusability

The used 2sNBG800 was collected by vacuum filtration, washed with ethanol and water, and resuspended into the fresh SAM solution. Afterwards, the procedure similar to the abovementioned for the evaluation of catalytic performance of 2sNBG was carried out. The analyses of XPS, FTIR and TGA were conducted for the 2sNBG 3rd run (the used 2sNBG after three consecutive cycles). The concentration of B element in the solution after each run was analyzed on the ICP mass spectrometer (PerkinElmer SCIEX, ELAN DRC-e).

3. Results and discussion

3.1. Characterization of carbocatalysts

3.1.1. 2sNBGs fabricated under selected T_a

Morphologies of 2sNBGs were investigated through FESEM and TEM. As shown in FESEM images (**Fig. 1(a)-(b)** and **Fig. S1(a)-(f)**), compared with GO with a silk veil-like structure, after thermal annealing and doping process, more exfoliation and wrinkles were created. The incorporation of N atoms induced more exfoliation and crumples than that of B atoms. The 2sNBG800 was found to be most exfoliated. The higher degree of exfoliation provides more active sites exposed for carbocatalysis. The partially aggregated and corrugated structure was obtained at the boundaries of the carbon network of 2sNBG800, originating from the structural distortion and the created defective sites after N, B-co-doping. Furthermore, the TEM images

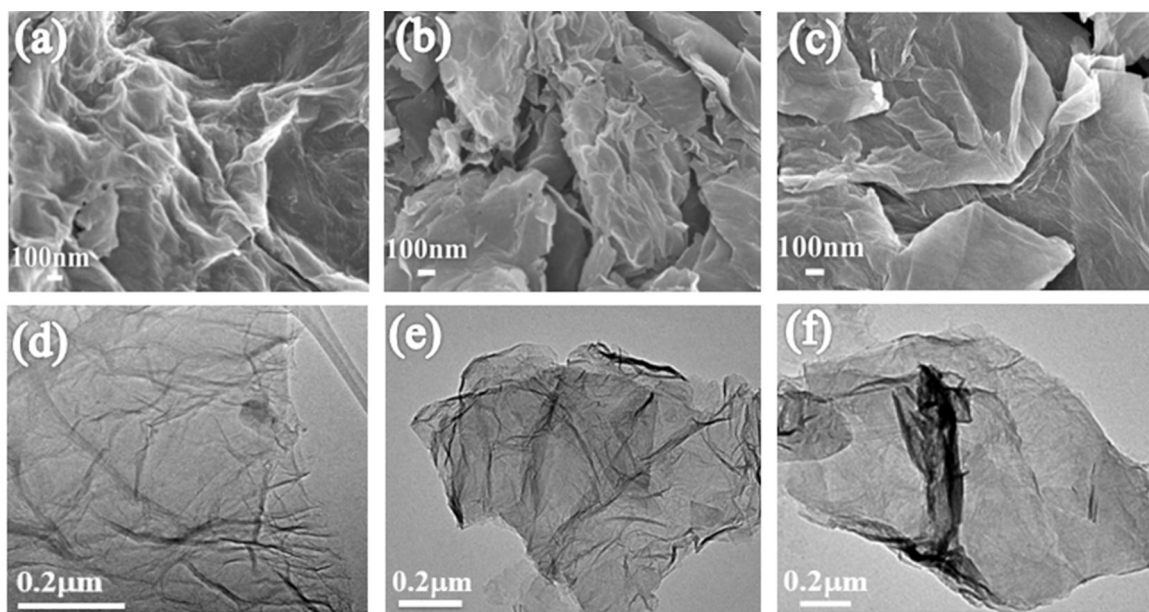


Fig. 1. FESEM images of NG600 (a), 2sNBG800 (b) and 1sNBG800 (c). TEM images of NG600 (d), 2sNBG800 (e) and 1sNBG800 (f).

(Fig. 1(d)–(e) and Fig. S1(g)–(h)) reveal that the characteristic 2D planar-like structure of graphene was still maintained after thermal annealing and doping. 2sNBG800 possessed more wrinkles and folding at the edges of graphitic sheets. The EDX elemental mappings of 2sNBG800 demonstrate the homogeneous distribution of the doped N and B atoms over the carbon network of 2sNBG800 (Fig. S2(a)–(e)).

The XRD patterns of 2sNBGs are shown in Fig. 2(a). After thermal annealing and doping, the characteristic strong (002) peak at $2\theta = 10^\circ$ (the corresponding interlayer spacing = 0.854 nm) in the XRD pattern of GO completely disappeared, whereas a new broad peak at $\sim 26^\circ$ (graphene (002) crystal plane) appeared in the XRD patterns of rGO800, NG600, BG800 and 2sNBGs, which suggests the exfoliation

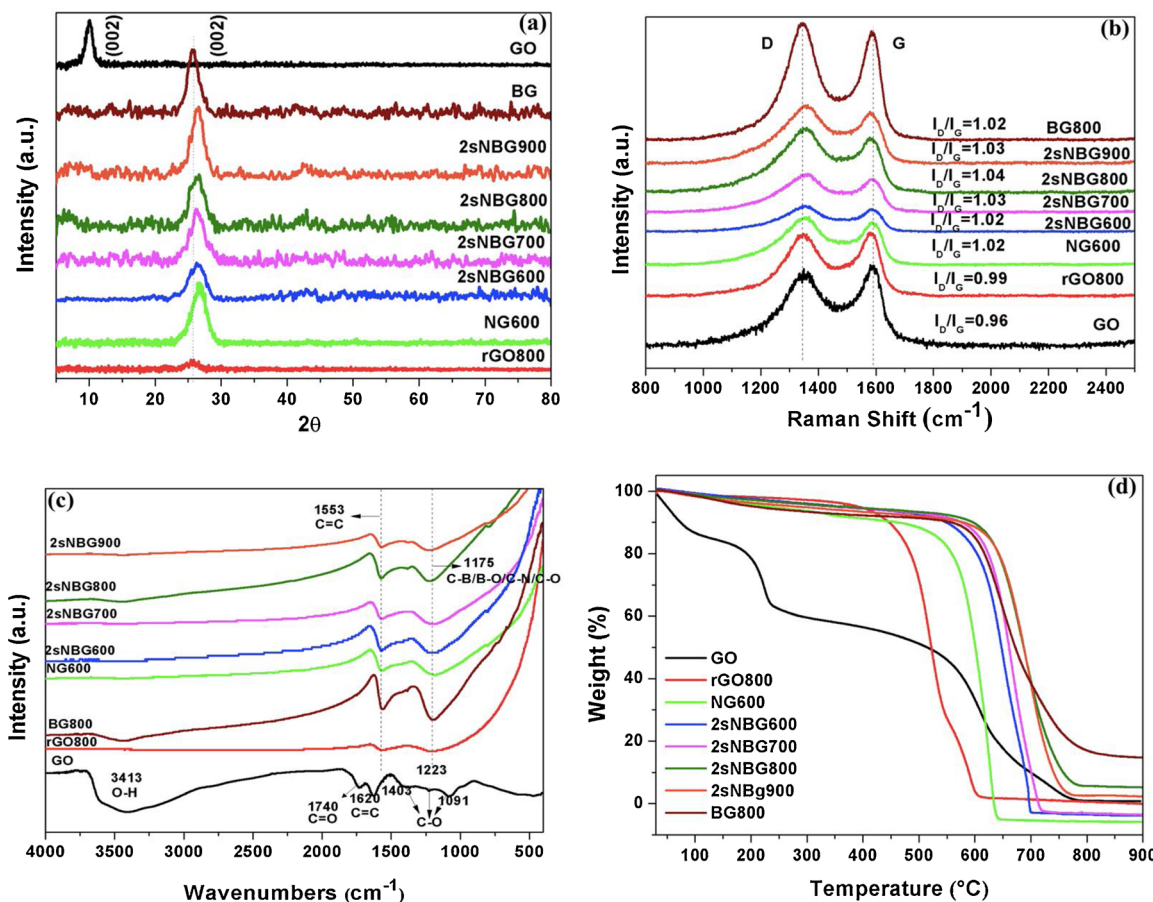


Fig. 2. (a) XRD patterns, (b) Raman spectra, (c) FTIR spectra and (d) TGA curves of GO, rGO800, BG800, NG600 and 2sNBGs.

Table 1a

Structural and chemical information of GO, rGO, NG, NBGs and BG.

	C at.%	O at.%	N at.%	B at.%	O/C	N/C	B/C	N/B	I_D/I_G
GO	53.2	42.8	—	—	0.80	—	—	—	0.96
rGO800	88.5	11.5	—	—	0.13	—	—	—	0.99
NG600	77.9	11.6	10.4	—	0.15	0.13	—	—	1.02
2sNBG600	80.4	7.8	10.2	1.6	0.10	0.13	0.02	6.38	1.02
2sNBG700	72.6	9.9	11.0	6.5	0.14	0.15	0.09	1.70	1.03
2sNBG800	56.6	13.2	13.8	16.3	0.23	0.24	0.29	0.84	1.04
2sNBG900	58.7	13.7	12.5	15.1	0.23	0.21	0.26	0.83	1.03
1sNBG800	53.2	15.9	13.3	17.6	0.30	0.25	0.33	0.76	1.12
BG800	84.9	11.6	—	3.4	0.14	—	0.04	—	1.02

Atomic percentages of C, O, N and B were analyzed by XPS.

and reduction (removal of oxygen-containing functional groups) of GO. Negligible influence on the crystalline structure of graphene was caused by the doping treatment [36]. Compared with rGO800 (25.9° , 0.335 nm) and BG800 (26.0° , 0.334 nm), the peaks of NG600 (26.7° , 0.325 nm) and 2sNBGs ($\sim 26.3^\circ$, 0.330 nm) shifted to a higher 2θ degree, which indicates that more reduction and exfoliation can be induced by N doping using urea as a nitrogen source, whereby urea can act as an expansion-reduction agent [37].

Raman spectra can provide further information on the structure of 2sNBGs. Two remarkable peaks at $\sim 1350\text{ cm}^{-1}$ (D-band) and $\sim 1580\text{ cm}^{-1}$ (G-band) correspond to the disorder content and graphitic symmetry, respectively, were observed in all the Raman spectra. The intensity ratio of D- to G-band (I_D/I_G) is closely related to the level of disorder of carbocatalysts. Fig. 2(b) and Table 1a show thermal annealing (I_D/I_G of rGO800: 0.99) and doping processes can increase the defective degree of GO (I_D/I_G of GO: 0.96). Compared with single N doping (1.02) or B doping (1.02), N, B-co-doping (2sNBGs: 1.02–1.04), especially at a high T_a , can further increase the I_D/I_G ratio, which can be explained as follows: 1) the difference in the bond distance between C-N/C-B and C-C enhanced the asymmetry of electron distribution in the graphitic domain, further indicating the successful incorporation of N and B heteroatoms [25]; 2) more defective sites (e.g., zigzag/armchair edges and vacancies) were generated by reduction and doping; and 3) smaller-size graphitic nanosheets were created [38]. 2sNBG800 had the highest defective level ($I_D/I_G = 1.04$).

FTIR can be employed to study the functional groups of 2sNBGs. As shown in Fig. 2(c), after thermal reduction and doping, the peak of C=C bond shifted from 1620 cm^{-1} of GO to 1553 cm^{-1} of rGO800, NG600, BG800 and 2sNBGs. Besides, a new broad peak centered at $\sim 1175\text{ cm}^{-1}$ was found in the FTIR spectra of rGO800, NG600, BG800 and 2sNBGs, which is ascribed to C-N/C-B/B-O/residue C-O bonds [39–41]. Notably, BG800 still maintained the broad peak centered at 3413 cm^{-1} (associated with the H_2O adsorption or O-H stretching), which implies that B doping can improve the hydrophilicity of rGO.

Table 1b
XPS deconvolution information of NG, NBGs and BG.

	pyridinic N $N_{\text{pyridinic-}}/N_{\text{total}}\text{ (%)}$	pyrrolic N $N_{\text{pyrrolic-}}/N_{\text{total}}\text{ (%)}$	graphitic N $N_{\text{graphitic-}}/N_{\text{total}}\text{ (%)}$	N of h-NB $N_{\text{h-NB}}/N_{\text{total}}\text{ (%)}$	BC3 $B_{\text{BC3}}/B_{\text{total}}\text{ (%)}$	$\text{BC2O}/\text{BCO2}$ $B_{\text{BC2O or BCO2}}/B_{\text{total}}\text{ (%)}$	$\text{B-O}/\text{B}_{\text{B-O}}$ $B_{\text{total}}\text{ (%)}$	B of h-NB $B_{\text{h-NB}}/B_{\text{total}}\text{ (%)}$
NG600 ^a	34.5	21.7	30.8	—	—	—	—	—
2sNBG600	28.5	39.7	31.7	—	7.0	57.8 (BC2O)/35.2(BCO2)	—	—
2sNBG700	55.6	16.4	28.0	—	25.6	41.4(BC2O) /33.0(BCO2)	—	—
2sNBG800	73.4	23.2	3.4	—	43.4	56.6(BC2O)	—	—
2sNBG900	64.0	30.2	5.8	—	34.9	65.1(BC2O)	—	—
1sNBG800	43.4	18.4	7.8	30.4	17.2	29.0(BC2O) /20.9(BCO2)	—	32.8
BG800	—	—	—	—	21.1	—	78.9	—

Atomic percentages of pyridinic N, pyrrolic N, graphitic N, h-NB, BC3, BC2O/BCO2 and B-O were analyzed by XPS.

^a NG600 still contained nitric oxide (13.0 at.%) ($N_{\text{nitric oxide}}/N_{\text{total}}$) apart from pyridinic N, pyrrolic N and graphitic N, while other carbocatalysts in the Table 1b just contained pyridinic N, pyrrolic N and graphitic N in the high resolution N1s spectrum.

TGA can be used to explore the thermal stability of 2sNBGs. As shown in Fig. 2(d), all the carbocatalysts (rGO800, NG600, BG800 and 2sNBGs) processed by thermal annealing and doping demonstrated enhanced thermo-oxidative stability of up to 500°C in air, which suggests the existence of the well-ordered graphitic carbon framework in those carbocatalysts [42]. After N, B-co-doping, the thermal stability of all the 2sNBGs was improved in comparison to that of rGO800, NG600 and BG800, especially at the high T_a . The substituted B atoms in the graphitic carbon framework (BC3) has been documented to be capable of promoting the graphitization and suppressing the oxidation [43]. Hence, the formation of BC3 can reinforce the sp^2 graphitic carbon framework, which is commensurate with the following XPS analysis of 2sNBG800 with the highest level of BC3 (43.4 at.%, $B_{\text{BC3}}/B_{\text{total}}$) (Table 1b and Fig. 3(b)) and the resultant high thermal stability of 2sNBG800. Notably, $\sim 15\text{ wt.\%}$ residual can be detected in the BG800 TGA curve after combustion at 900°C in air. It has been reported that the combustion sites can be blocked by B doping, which retards the oxidation of graphitic carbons even at the elevated T_a [44–46]. Compared with rGO800, the relatively higher initial weight loss of BG800 can be attributed to the evaporation of absorbed water, which is commensurate with the obvious broad peak detected at $\sim 3413\text{ cm}^{-1}$ in the FTIR spectrum of BG800 (Fig. 2(c)) and further confirms the B doping can promote the hydrophilicity of rGO [36].

The chemical compositions of 2sNBGs were acquired from XPS analysis (Fig. S3(m)). The detailed information is shown in Table 1a. After incorporation of B atoms into NG600, the atomic ratio of N/C of 2sNBGs increased from 0.13 to 0.24 with an increase in T_a from 600 to 800°C , then slightly decreased at 900°C (N/C = 0.21). The atomic ratio of B/C of 2sNBGs raised from 0.02 to 0.29 with the elevated T_a from 600 to 800°C , whereas the atomic ratio of B/C of 2sNBG900 was slightly reduced to 0.26, exhibiting the similar trend to that of N/C. The reduction of the atomic ratios of N/C and B/C in 2sNBG900 results from the breakup of C-N and C-B bond at a high T_a [29]. The raised T_a induces a relatively greater increase in B/C ($\Delta = 0.27$) than that of N/C ($\Delta = 0.11$), which implies that the higher T_a facilities B doping into NG. Among all the 2sNBGs, 2sNBG800 had the highest level of N (13.8 at.%) and B (16.3 at.%).

The XPS N1s fitting (394–407 eV) was obtained for all the 2sNBGs (Fig. S3(a)(c)(e)(g)). The detailed information is shown in Table 1b and Fig. 3(a). The most common N bonding configurations include pyrrolic N (N in a 5-membered heteroring, 398.76–400.3 eV), pyridinic N (N in a 6-membered heteroring on the edges, 397.95–399 eV) and graphitic N (sp^2 hybridized N adjacent to three sp^2 C atoms, 400.9–401.7 eV) [23]. All three categories of N species were identified in the 2sNBGs. However, the typical N (397.6–397.9 eV) in h-BN [29,47,48] was not detected. It was reported that, with the elevated T_a , the content of pyridinic N and pyrrolic N of NG would decrease in NG, while the content of graphitic N would increase due to the better thermal stability [12]. However, a different scenario occurs for two-step

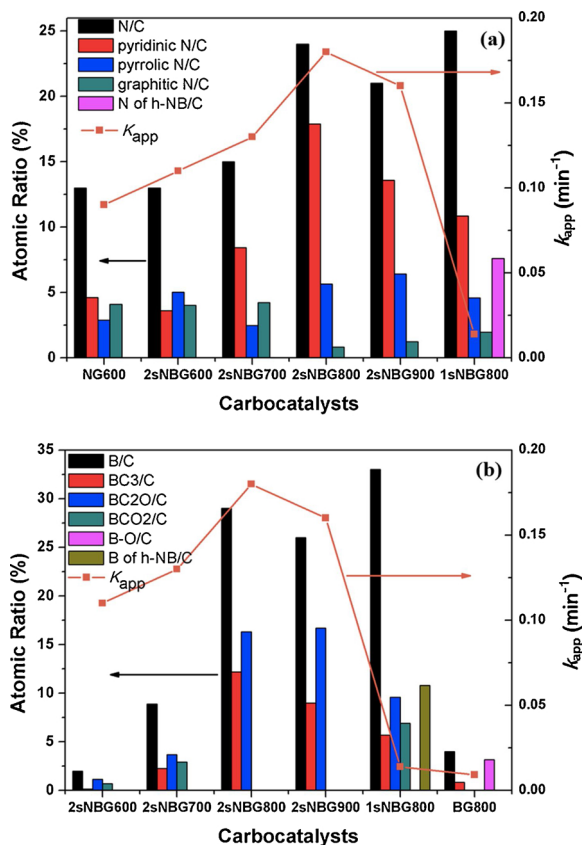


Fig. 3. The doing level and the concentration of bonding configuration of N dopant (a) and B dopant (b) in 2sNBGs, 1sNBG800, NG600 and BG800, and their influence on k_{app} (catalytic activity) of the carbocatalysts.

N, B-co-doping. The content of pyridinic N increased from 28.5 to 73.4 at.% ($N_{pyridinic-N}/N_{total}$) with an increase in T_a from 600 to 800 °C, whereas 2sNBG900 had a slightly reduced pyridinic N content of 64.0 at.% ($N_{pyridinic-N}/N_{total}$). By contrast, the content of graphitic N decreased from 31.7 to 3.4 at.% ($N_{graphitic-N}/N_{total}$) with the elevated T_a from 600 to 800 °C, while 2sNBG900 had a slightly increased graphitic N content of 5.8 at.% ($N_{graphitic-N}/N_{total}$), which suggests that the sequential incorporation of B atoms can induce the conversion of N bonding configurations in NG [26,30]. 2sNBG800 had the highest level of pyridinic N (73.4 at.%, $N_{pyridinic-N}/N_{total}$).

The XPS B1s fitting (184–200 eV) was obtained for all the 2sNBGs (Fig. S3(b)(d)(f)(h)). The detailed information is displayed in Table 1b and Fig. 3(b). The B signals can be deconvoluted into BC3 (189–190 eV), B of h-BN (190.6–191 eV), B-C-O (BC2O/BCO2) (191–192 eV) and B-O (192–193 eV) [23,25,48,49]. BC3 and BC2O/B-

BCO2 were detected for all the 2sNBGs. The B in h-BN was barely detected. The content of BC3 increased from 7.0 to 43.4 at.% (B_{BC3}/B_{total}) with the elevated T_a from 600 to 800 °C, and decreased slightly to 34.9 at.% (B_{BC3}/B_{total}) at 900 °C, which follows the similar trend to that of pyridinic N and implies that the high T_a can facilitate the substitutional doping of B. 2sNBG800 had the highest level of BC3 (43.4 at.%, B_{BC3}/B_{total}). No B-O bond was detected for all the 2sNBGs, whereas 78.9 at.% (B_{B-O}/B_{total}) of B–O existed in BG800, which is ascribed to the large amount of oxygen functional groups in GO and the high T_a [23,25,50].

Table 2 and Fig. S4(a) and (b) show the textural properties of 2sNBGs. The lowest SSA ($26 \text{ m}^2 \text{ g}^{-1}$) of GO is attributed to the significant stacking effect caused by a strong hydrogen bond (attractive interaction between the surface oxygen-containing functionalities of GO). However, SSA can be dramatically increased after the thermal annealing. The highest SSA value ($450 \text{ m}^2 \text{ g}^{-1}$) of rGO800 results from the elimination of the oxygen-containing functionalities on the GO layers and thermal expansion resulted from thermal annealing. The incorporation of N or B atoms can reduce the SSA from $450 \text{ m}^2 \text{ g}^{-1}$ of rGO to $51\text{--}84 \text{ m}^2 \text{ g}^{-1}$ of N, B single/co-doped graphene, which can be associated with the disorientation and corrugation of graphitic basal planes due to the introduction of dopants [51]. The elevated T_a slightly increased the SSA value of 2sNBGs from 51 to $62 \text{ m}^2 \text{ g}^{-1}$. 2sNBG800 possessed the highest SSA value of $62 \text{ m}^2 \text{ g}^{-1}$ among all the 2sNBGs. All the carbocatalysts in this study are mainly comprised of mesopores (distribution of pore radius mainly centered at $\sim 2 \text{ nm}$).

3.1.2. Comparison between 1sNBG and 2sNBG

Compared with 2sNBG800, FESEM (Fig. 1(c)) and TEM (Fig. 1(f)) images of 1sNBG800 both demonstrate 1sNBG800 still maintained the planar 2D structure of graphene. However, 1sNBG800 was less wrinkled albeit with more random aggregation of layers, which has been documented in the case of h-BN nanosheets [52] and is related to the relatively lower SSA of 1sNBG800 ($30 \text{ m}^2 \text{ g}^{-1}$) (Table 2). EDX elemental mappings of 1sNBG800 (Fig. S2(f)–(j)) demonstrate that N and B heteroatoms were uniformly distributed across the sheets of 1sNBG.

As shown in Table 1a, in comparison to 2sNBG800 (the atomic ratio of N/C: 0.24, B/C: 0.29 and O/C: 0.23), 1sNBG800 had a relatively higher level of N (N/C: 0.25), B (B/C: 0.33) and O (O/C: 0.30) in its XPS spectrum (Fig. S3(m)). Table 1b, Fig. 3 and Figs. S3(k) and (l) show that 30.4 at.% N of h-BN (N_{h-NB}/N_{total}) can be detected apart from pyridinic N (43.4 at.%, $N_{pyridinic-N}/N_{total}$), pyrrolic N (18.4 at.%, $N_{pyrrolic-N}/N_{total}$) and graphitic N (7.8 at.%, $N_{graphitic-N}/N_{total}$) in 1sNBG800. By contrast, 2sNBG800 had a higher level of pyridinic N (73.4 at.%, $N_{pyridinic-N}/N_{total}$) and none of N of h-BN. Similarly, 32.8 at.% B of h-BN (B_{h-NB}/B_{total}) can be detected besides BC3 (17.2 at.%, B_{BC3}/B_{total}) and BC2O (29.0 at.%) (B_{BC2O} or B_{CO2}/B_{total}) in 1sNBG800. By contrast, 2sNBG800 had a higher BC3 (43.4 at.%, B_{BC3}/B_{total}) content and none of B of h-BN.

As shown in Fig. 4(a), the XRD pattern of 1sNBG800 is similar to that of 2sNBG800 ($2\theta = 26.3^\circ$, 0.330 nm) with a strong peak at $2\theta = 26.8^\circ$ (0.324 nm), which cannot exclude the existence of h-BN in 1sNBG800. This is because the (002) orientation of h-BN nanosheets corresponds to the characteristic peak at $2\theta = 26.8^\circ$ [52,53] and the crystalline h-BN is less likely to form at 800 °C [54]. As shown in Fig. 4(b) and Table 1a, 1sNBG800 exhibited the highest I_D/I_G ratio (1.12) among all the carbocatalysts in this study with a wider D band, which indicates the formation of h-BN [25]. It has been reported that the two characteristic FTIR peaks of h-BN are $\sim 1390 \text{ cm}^{-1}$ (in-plane bending) and $\sim 780 \text{ cm}^{-1}$ (out-of-plane stretching). Thus, the two strong peaks (1375 and 755 cm^{-1}) in the FTIR spectrum of 1sNBG800 (Fig. 4(c)) further confirm the formation of h-BN/NBG hybrid. TGA curve of 1sNBG800 (Fig. 4(d)) exhibits that, among all the carbocatalysts in this study, the oxidation of 1sNBG800 was significantly retarded (46 wt% residual after combustion at 900 °C in air), which is associated with the high thermal stability of h-BN (up to 2950 °C) [52,53] and commensurate with the FTIR result. Around 30 wt.% weight loss of

Table 2
SSA, pore volume and pore size information of GO, rGO, NG, NBGs and BG.

Catalyst	BET SSA ($\text{m}^2 \text{ g}^{-1}$)	Average pore volume ^a ($\text{cm}^3 \text{ g}^{-1}$)	Average pore size ^b (nm)
GO	26	0.017	2.03
rGO800	450	0.439	2.02
NG600	51	0.102	2.01
2sNBG600	51	0.110	2.03
2sNBG700	55	0.116	2.03
2sNBG800	62	0.122	2.02
2sNBG900	61	0.109	2.02
1sNBG800	30	0.048	2.02
BG800	84	0.104	2.02

^a BJH method cumulative desorption pore volume.

^b BJH method desorption pore radius (Mode $D_v(r)$).

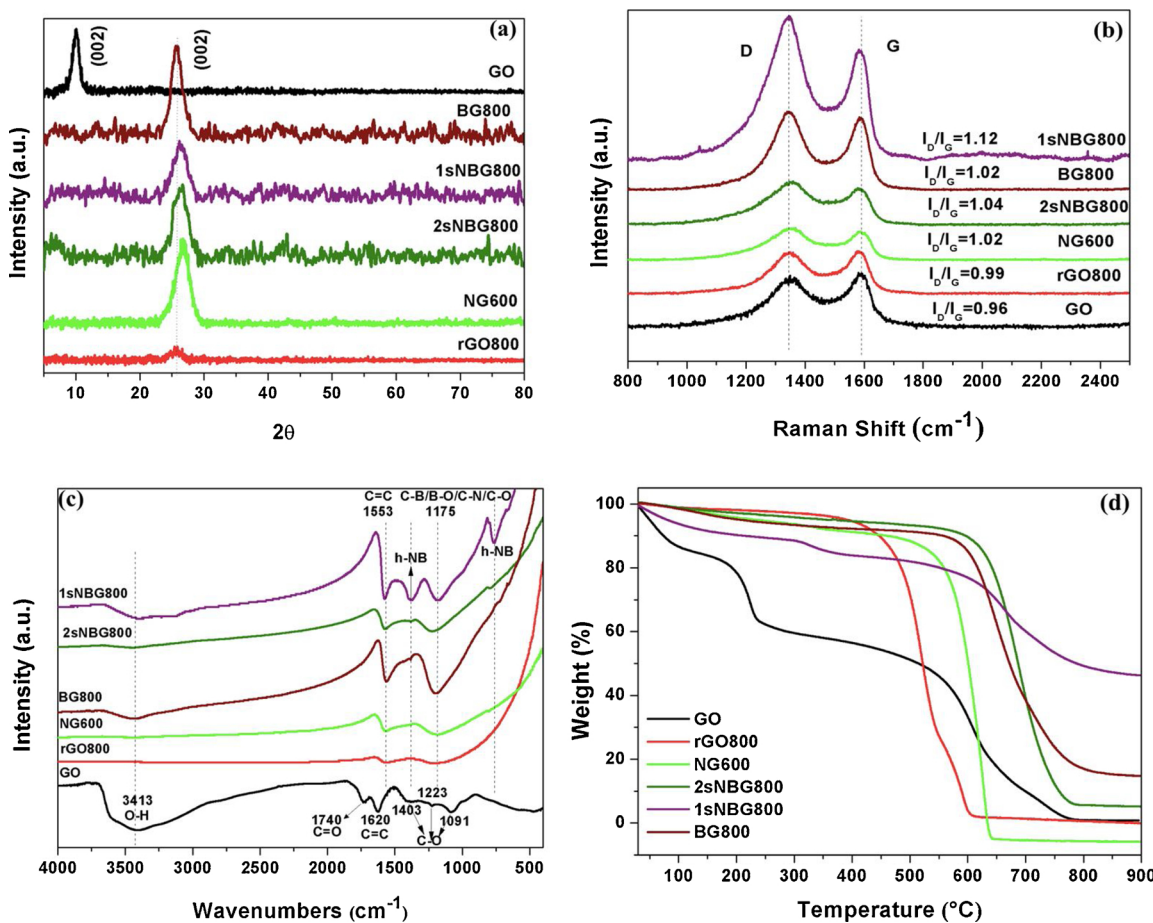


Fig. 4. Comparison between 1sNBG800 and 2sNBG800 in (a) XRD patterns, (b) Raman spectra, (c) FTIR spectra and (d) TGA curves.

1sNBG800 below 600 °C can be attributed to the desorption of absorbed water in the interspace between h-BN and graphene sheets [53]. As shown in Table 2 and Fig. S4, 1sNBG800 had a lower SSA ($30 \text{ m}^2 \text{ g}^{-1}$) and mediocre pore volume ($0.048 \text{ cm}^3 \text{ g}^{-1}$) in comparison to those of 2sNBG800 ($62 \text{ m}^2 \text{ g}^{-1}$ and $0.122 \text{ cm}^3 \text{ g}^{-1}$), which can be associated with the formation of h-BN.

Thus, results of the above characterization of 1sNBG800 and 2sNBG indicate that one-step thermal annealing (simultaneous incorporation of N and B heteroatoms) leads to the formation of h-BN (by-product)/NBG hybrid (the structure shown in the inset of Fig. S3(k)). However, two-step thermal annealing (sequential incorporation of N and B) results in the h-BN-free NBG. From the thermodynamic perspective, there is a tendency for the separation of C-rich domain and BN-rich domain [55]. However, the kinetics of a specific synthesis method usually controls the formation of N-B bonding configurations, leading to the possible existence of B-C-N heteroring [56]. The kinetics of a specific synthesis are comprehensively determined by the synthesis parameters (e.g., precursor, temperature, flow rate, in situ generated gas, etc.) [57], which account for the differences in the N-B bonding configurations caused by one-step and two-step thermal annealing methods used in this study. Besides, in one-pot synthesis, the direct interaction between urea and H_3BO_3 can also induce the formation of h-BN. Further efforts can be dedicated to the role of those abovementioned synthesis parameters in formation of N-B bonding structures.

3.2. Catalytic performance of NBGs

The catalytic activity of NBGs was evaluated in the catalytic activation of PMS to degrade aqueous SAM. Generally, less than 10% of SAM could be adsorbed within 60 min by the carbocatalysts except for

rGO800 (Table S1 and Fig. S5(a)). rGO800 can adsorb 35% SAM within 60 min, which is associated with its high SSA value of $450 \text{ m}^2 \text{ g}^{-1}$ (Table 2 and Fig. S4) and surface functionalities conducive to adsorption. The SSA of NG600, BG800 and 2sNBGs are in the same range from 51 to $84 \text{ m}^2 \text{ g}^{-1}$, whereas 1sNBG800 had the relatively low SSA of $30 \text{ m}^2 \text{ g}^{-1}$ (Table 2 and Fig. S4). The poor adsorption capacity of the doped graphene is associated with their relatively low SSA and reduced π - π interactions with SAM, attributed to the alteration of surface chemistry and lattice distortion by the incorporation of the dopants.

3.2.1. PMS-activating ability of 2sNBGs fabricated under selected T_a

The catalytic activities of 2sNBGs prepared under selected T_a are shown in Fig. 5(a). The pseudo first-order kinetics was used to estimate the apparent rate constant (k_{app}) of SAM removal on carbocatalysts through PMS activation, as shown in Eq. (1):

$$\ln\left(\frac{C}{C_0}\right) = -k_{app} t \quad (1)$$

where the initial SAM concentration is represented by C_0 and the SAM concentration at time t is represented by C . GO (0.009 min^{-1}) and BG800 (0.009 min^{-1}) can hardly activate PMS with only ~40% SAM removal within 60 min (Table S1). It has been reported that substitutional B atoms (BC3) (21.1 at.%, B_{BC3}/B_{total} in BG800) (Table 1b and Fig. 3(b)) tend to lower the electron density of the graphitic nanocarbon network [58]. Besides, the inactivity of B–O bond (78.9 at.%, B_{B-O}/B_{total} in BG800) (Table 1b and Fig. 3(b)) has been documented [23]. Thus, B doping (BG800) resulted in a suppression of PMS activation. rGO800 exhibited 76% SAM removal within 60 min (0.020 min^{-1}), primarily attributed to its outstanding adsorption

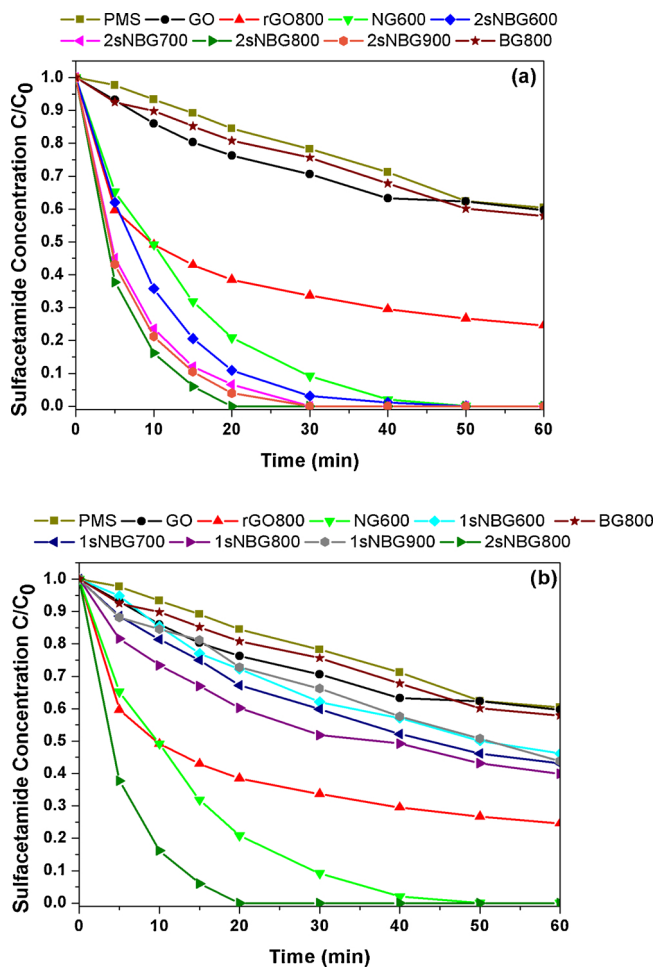


Fig. 5. Catalytic performances of (a) 2sNBGs and (b) 1sNBGs to activate PMS for SAM degradation (Condition: [PMS] = 0.5 mM, [SAM] = 10 mg L⁻¹, [catalyst] = 0.2 g L⁻¹, pH = 7).

ability (Fig. 5(a) and Table S1). NG600 achieved 100% removal of SAM within 50 min (the catalytic activity of NG800 (0.071 min^{-1}) was lower than that of NG600 (0.090 min^{-1})) (Fig. S5(b) and Table S1). However, all the 2sNBGs outperformed NG600 in terms of catalytic activity and followed the order of 2sNBG800 (0.182 min^{-1}) > 2sNBG900 (0.161 min^{-1}) > 2sNBG700 (0.133 min^{-1}) > 2sNBG600 (0.110 min^{-1}) > NG600 (0.090 min^{-1}) (Table S1). Given that the SSA of 2sNBGs is in the same range of $51\text{--}61 \text{ m}^2 \text{ g}^{-1}$ (Table 2 and Fig. S4), the catalytic performance of 2sNBGs is probably dominated by active sites rather than SSA. 2sNBG800 performed best to activate PMS for SAM degradation, inducing 20-, 9- and 2-fold improvements over GO, rGO800 and NG600, respectively. The order of catalytic capability of 2sNBGs followed the similar trend of the changes in the contents of pyridinic N and BC3 of 2sNBGs with the elevated T_a (Fig. 3).

The best catalytic performance of 2sNBG800 can be explained as follows:

- 1) The separated N atoms (not linked to B) can boost the catalytic activity of 2sNBG800 as they did in NG600 via the non-radical pathway to form surface activated species [12,14].
- 2) Compared with single N doping, the synergistic coupling effect between N and B atoms, especially synergy between pyridinic N and BC3, can contribute to the enhanced catalytic activity of 2sNBG (Section 3.3). Besides, the inactivity of B-C-O bond (BC2O/BCO₂) has been reported in oxygen reduction [25]. 2sNBG800 possessed the highest levels of N (13.8 at.%) and B (16.3 at.%), the highest contents of pyridinic N (73.4 at.%, N_{pyridinic-N}/N_{total}) and BC3 (43.4

at.%, B_{BC3}/B_{total}), the lowest B-C-O content (56.6 at.% BC2O, B_{BC2O}/B_{total}), and none of h-BN (Table 1 and Fig. 3). The optimal surface chemistry secures its highest catalytic activity for PMS activation to degrade SAM.

3) 2sNBG800 had the highest I_D/I_G ratio of 1.04 (Fig. 2(b) and Table 1a) among all the 2sNBGs, indicating that rich defective sites have been created in 2sNBG800. It has been reported that zigzag/armchair edges can activate PMS by cleaving the peroxide O-O bond for the generation of SO_4^{2-} and HO^\cdot , whereas the vacancies are more capable of adsorbing PMS to form a surface complex with fewer transfer electrons from graphitic lattice to PMS to coordinate the non-radical oxidation [59].

An increase in PMS dosage (leading to enhanced interactions between PMS and 2sNBG800) or catalyst loading of 2sNBG800 (more active sites brought in for PMS activation) can further enhance the SAM degradation in the 2sNBG800/PMS/SAM system (Fig. S6(a) and (b)). However, comparing the slopes of the linear plots (the insets of Fig. S6(a) and (b)), the enhancement in SAM degradation efficiency caused by increasing catalyst loading is ~3 times higher than that caused by increasing PMS dosage. Given that recovering and recycling 2sNBG is easier than that of PMS, the increase in the catalyst loading operationally outperforms that of PMS dosage for the enhanced SAM degradation. Meanwhile, the downstream impact of residual PMS can be reduced. The catalytic activity of 2sNBG800 was also investigated for the degradation of other antibiotics (e.g., SNM, SMX and STZ) (Fig. S6(c)). These pollutants can be eliminated within 30 min by 2sNBG800/PMS, which suggests that 2sNBG can be used as a promising carbocatalyst to remove sulfonamides.

3.2.2. Comparison in catalytic performance between 1sNBGs and 2sNBGs

Fig. 5(b) demonstrates the catalytic performance of 1sNBG600, 1sNBG700, 1sNBG800 and 1sNBG900 as compared to that of 2sNBG800, NG600, rGO800 and GO. The SAM removal efficiency and k_{app} in 1sNBGs/PMS/SAM system fall between 54–60% within 60 min and 0.013–0.014 min⁻¹ (Table S1), respectively. Therefore, the elevated T_a did not induce a great difference in the catalytic activity of 1sNBGs. All the 1sNBGs performed worse than NG600 with 100% SAM removal (reaction time = 50 min, $k_{app} = 0.090 \text{ min}^{-1}$) (Table S1). The catalytic performance of all the doped carbocatalysts employed in this study follows the order of 2sNBGs > NG600 > 1sNBGs > BG800. The poor catalytic performance of 1sNBG800 can be explained as follows: 1) 1sNBG800 has been demonstrated to be a h-BN/graphene hybrid according to its characterization analysis in this study. h-BN has been reported to be chemically inert [53], which is caused by the neutralization between bonded N and B atoms. Specifically, the vacant orbital of B atom can be significantly neutralized by the lone-pair electrons of the adjacent N atom, which leads to looser electron density to conjugate with the free-flowing π -electrons from sp^2 carbons in graphene [49]; and 2) the relatively lower SSA of 1sNBG800 ($30 \text{ m}^2 \text{ g}^{-1}$) (Table 2 and Fig. S4) results in limited access to active sites for PMS activation. Therefore, the two-step strategy in this study successfully limited the formation of h-BN, giving rise to maneuvered and favorable N-B bonding configurations (especially pyridinic N and BC3) for PMS activation.

3.3. Mechanism of PMS activation in the 2sNBG800/PMS/SAM system

3.3.1. Quenching experiments

Generally, radical and non-radical oxidation are two main catalytic oxidation pathways involved in the carbocatalyst/PMS system. Radical oxidation relates to the scission of the peroxide O-O bond in PMS to SO_4^{2-} and HO^\cdot . The radical production can be promoted by 1) defective sites (e.g., zigzag/armchair edges, vacancies) on the carbocatalysts; 2) a lone pair of electrons from Lewis basic sites (e.g., pyrrolic N, pyridinic N, etc.); and 3) conjugation between the lone-pair electrons of dopants

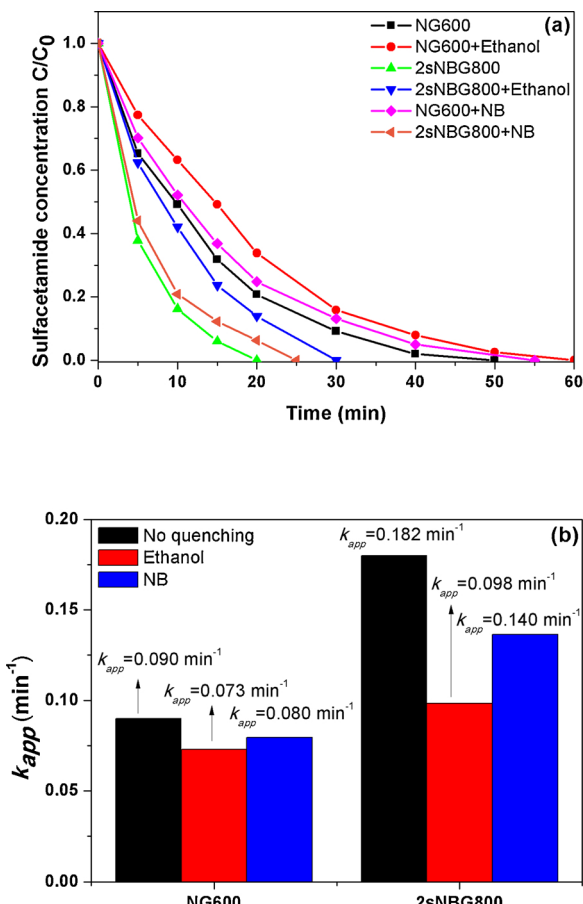


Fig. 6. The effect of ethanol and NB as quenching agents on the SAM removal (a) and SAM degradation rate (b) in the NG600/PMS/SAM and 2sNBG800/PMS/SAM systems (Condition: [PMS] = 0.5 mM, [SAM] = 10 mg L⁻¹, [catalyst] = 0.2 g L⁻¹, pH = 7, [ethanol] = 1.5 M, [NB] = 25 mg L⁻¹).

and the homogeneous π -electron system of sp^2 carbons. On the other hand, non-radical oxidative reaction is a surface-confined process via an electron-transfer regime, which usually exhibits a relatively mild oxidative potential [60,61]. In the NG/PMS system, the higher electronegativity of graphitic N than that of the adjacent carbon atoms (χ_N (3.04) > χ_C (2.55)) can lead to the formation of active sites comprising negatively charged N and positively charged C, thus facilitating the

generation of surface activated species via strong electrostatic bonds with PMS [12,14].

Ethanol and NB have been selected to probe the possible catalytic mechanism of PMS activation in the NG600/PMS/SAM and 2sNBG800/PMS/SAM systems. Ethanol can be used to scavenge both SO_4^{2-} and HO^\cdot ($k_{SO_4^{2-}+ethanol} = 10^7 \text{ M}^{-1} \text{ s}^{-1}$, $k_{HO^\cdot+ethanol} = 10^9 \text{ M}^{-1} \text{ s}^{-1}$). NB can serve as a quenching agent for HO^\cdot ($k_{HO^\cdot+N} (3.9 \times 10^9 \text{ M}^{-1} \text{ s}^{-1}) > k_{SO_4^{2-}+N} (< 10^6 \text{ M}^{-1} \text{ s}^{-1})$) [10].

As shown in Fig. 6, in the NG600/PMS/SAM system, 1.5 M ethanol led to 20% reduction in k_{app} , while 25 mg L⁻¹ NB did not exert a significant influence in the SAM degradation (11% reduction in k_{app}). By contrast, in the 2sNBG800/PMS/SAM system, 45% and 24% decreases in k_{app} were induced by 1.5 M ethanol and 25 mg L⁻¹ NB, respectively. 1.5 M ethanol (molar ratio of ethanol: PMS = 3000 : 1) can effectively quench radicals produced in the Co^{2+} /PMS/SAM system (87% reduction in k_{app}) (Fig. S7), which is well known as a pure radical based system [62]. Thus, it indicates that NG600/PMS/SAM is a non-radical-dominated system and the incorporation of B atoms into NG facilitates the transition of non-radical oxidation to radical oxidation in the 2sNBG800/PMS/SAM system. Both HO^\cdot and SO_4^{2-} partially contributed to the SAM oxidation in the 2sNBG800/PMS/SAM system.

3.3.2. Density functional theory (DFT) calculation

DFT calculation was conducted to further elucidate the catalytic mechanism in the single-doped graphene (NG or BG) and co-doped graphene (NBG) for PMS activation. Theoretical methodology is demonstrated in the Text S2. PMS activation process on different atomic structures of graphene before and after doping is shown in Fig. 7. Adsorption energy (E_{ads}) of PMS onto different graphene substrates, length of O-O bond (l_{O-O}) and electron transfer (Q) from carbon to PMS were calculated for different graphene structures before and after doping (Fig. S12 - Fig. S16, Table S4 - Table S8). As shown in the summary of Table 3, as for single doping and pristine graphene (G), the enhancement in the E_{ads} , l_{O-O} , and Q follows the order of graphitic N-doped graphene (NG-g) > BG > G > pyridinic N-doped graphene (NG-pd) ≈ pyrrolic N-doped graphene (NG-pl). As for N, B-co-doping models, the enhancement order is pyridinic N and B-co-doped graphene (NBG-pd) > graphitic N and B-co-doped graphene (NBG-g) > pyrrolic N and B-co-doped graphene (NBG-pl).

The NG-g manifests the longest l_{O-O} (1.475 Å) and most electron transfer (0.959 e), suggesting that PMS can be effectively activated. The strongest adsorption energy (E_{ads} = -2.468) implies that the activated PMS molecule will be intimately confined on the carbon surface to form surface reactive species (non-radical pathway) rather than releasing sulfate radicals.

Fig. 7. Atomic structures of graphene before and after doping: (a) pure graphene, (b) pyridinic N-doped graphene (NG-pd), (c) pyrrolic N-doped graphene (NG-pl), (d) graphitic N-doped graphene (NG-g), (e) boron-doped graphene (BG), (f) graphitic N and B-co-doped graphene (NBG-g), (g) pyridinic N and B-co-doped graphene (NBG-pd) and (h) pyrrolic N and B-co-doped graphene (NBG-pl). Color codes: the gray, white, blue and pink are carbon, hydrogen, nitrogen and boron atoms, respectively. The number indicates the possible arrangement of dopants.

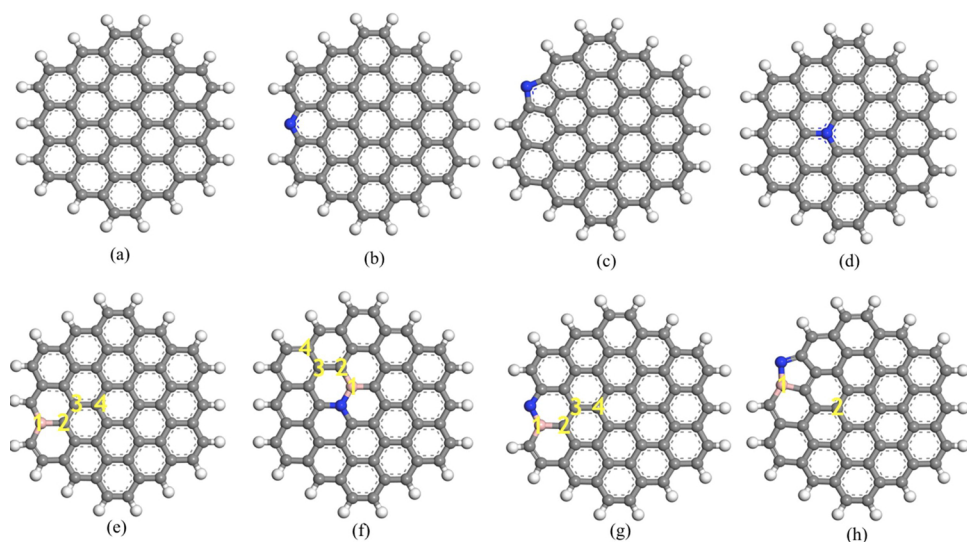


Table 3

PMS adsorption onto different models of graphene before and after doping.

Configuration	l_{O-O} (Å)	Q(e)	E_{ads} (eV)
Free PMS	1.332	—	—
G	1.420	0.617	-0.909
BG	1.428	0.632	-0.867
NG-pd	1.414	0.573	-0.847
NG-pl	1.416	0.582	-0.836
NG-g	1.475	0.959	-2.468
^a NBG-pd-4	1.470	0.813	-1.721
^b NBG-pl-1	1.427	0.620	-0.922
^c NBG-g-4	1.451	0.765	-1.220

^a NBG-pd-4 refers to the B-C-C-C-pyridinic N structure (**Fig. 7(g)** and **Fig. S15**).

^b NBG-pl-1 refers to the B-pyrrolic N structure (**Fig. 7(h)** and **Fig. S16**).

^c NBG-g-4 refers to the B-C-C-C-graphitic N structure (**Fig. 7(f)** and **Fig. S14**).

NBG-pd-4 (4 indicates bonding configuration of B-C-C-C-pyridinic N, as shown in **Fig. 7(g)** and **Fig. S15**) also manifests a great performance for PMS activation with a prolonged peroxide O-O bond (1.470 Å vs 1.332 Å of free PMS) and a great electron transfer of 0.813 e from carbon to PMS. However, the E_{ads} is much smaller compared with NG-g, which indicates the potential to generate free radicals after the cleavage of peroxide O-O bonds (the radical pathway).

The charged densities of all the atoms in different graphene models were also calculated to gain further insights on the effect of introduction of dopants on the electron status of carbon atoms in the graphitic sheet (**Fig. S17-S22**). **Fig. 8** demonstrates molecular structure of NBG-pd-4. As shown in **Table 4**, the introduction of N can induce a higher positive charge density to the neighboring carbon atoms (C1 and C2) than that of B (C3, C4 and C5). Co-doping of B into NG in the position 4 (bonding configuration of B-C-C-C-pyridinic N) can further increase the positive charge density of carbon atoms (C1: 0.406 → 0.536, C3: 0.177 → 0.408, C4: -0.110 → 0.247, C5: 0.142 → 0.276).

In regard to the better experimental performance of 2sNBG compared with NG, the phenomenon can be explained in two aspects. Firstly, as aforementioned, the 2sNBG contains both sole N sites and N, B-co-doped domains, which will simultaneously induce radical and non-radical pathways which have already been evidenced by the

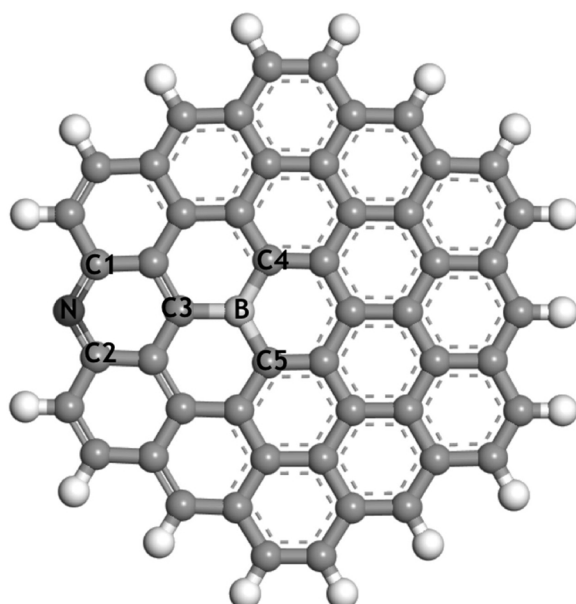


Fig. 8. Molecular model of NBG-pd-4 (4 indicates bonding configuration of B-C-C-pyridinic N). Color codes: the gray, white, blue and pink are carbon, hydrogen, nitrogen and boron atoms, respectively.

Table 4

Charge density of atoms in the graphitic sheet.

Atom number	Graphene	^a BG-4	^b NG-pd	^c NBG-pd-4
N	—	—	-0.854	-0.854
B	—	-1.045	—	-1.106
C1	-0.040	0.114	0.406	0.536
C2	-0.113	0.101	0.592	0.558
C3	-0.039	0.454	0.177	0.408
C4	0.124	0.222	-0.110	0.247
C5	0.186	0.235	0.142	0.276

^a BG-4 refers to B-doped graphene. 4 indicates the position of B atom in the graphitic sheet (**Fig. 7(e)** and **Fig. S13**).

^b NG-pd refers to pyridinic N-doped graphene (**Fig. 7(b)** and **Fig. S12**).

^c NBG-pd-4 refers to pyridinic N and B-co-doped graphene. 4 indicates the bonding configuration of B-C-C-C-pyridinic N (**Fig. 7(g)** and **Fig. S15**).

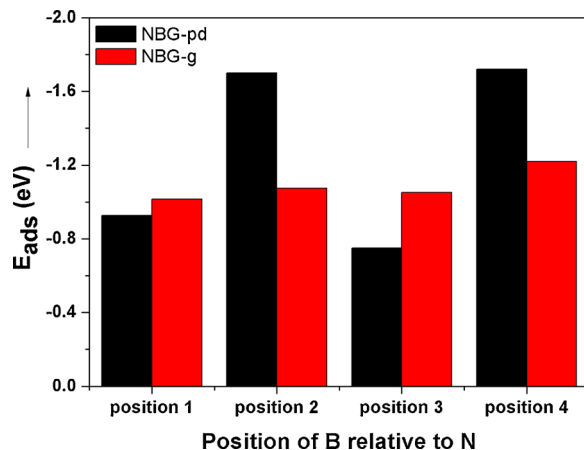


Fig. 9. The effect of position of B relative to N on the adsorption energy (E_{ads}) of NBG. Position 1, position 2, position 3 and position 4 refer to bonding configurations of B-N, B-C-N, B-C-C-N and B-C-C-C-N, respectively.

radical quenching tests (45% radical oxidation). The radical pathway is a homogeneous reaction which further accelerates the oxidation. More importantly, the N, B-co-doping can bring in more positively charged carbons in the graphene lattice, suggesting that more catalytic centers are generated for binding with the negatively charged oxygen atoms in PMS.

In addition, as shown in **Fig. 9**, the two most reactive N dopants (pyridinic N and graphitic N) and their distances with B atom can induce different functions. Pyridinic N interacting with B in the position 2 (B meta to N, B-C-pyridinic N, $E_{ads} = -1.70$ eV) or 4 (B-C-C-C-pyridinic N, $E_{ads} = -1.72$ eV) demonstrate a higher E_{ads} , whereas the lower E_{ads} (-0.926 ~ -1.016 eV) was found when B is in position 1 (B ortho to N, B-N) for both pyridinic N and graphitic N. This DFT result explained the experimental phenomenon that the existence of h-BN deteriorated the performance of 1sNBG catalyzed PMS activation.

In summary, DFT results theoretically verifies the experiment-derived order of catalytic activities: 2sNBGs > NG600 > 1sNBGs > BG800. The N, B-co-doping is highly reactive for PMS activation with a moderate adsorption energy, which is different from the single-graphitic N doping with strong adsorption. This suggests that intermediate of NBG/PMS is prone to be detached to induce a radical process (SO_4^{2-} or HO^{\cdot}). Types of N dopant and distance between N and B atoms significantly influence the charge density distribution of the carbon lattice, and therefore the catalytic activity of NBG. The synergistic coupling effect between pyridinic N and BC3 in the bonding configuration of B-C-C-C-pyridinic N can induce more positively charged carbon atoms as active sites, which boost the catalytic activity of 2sNBG for PMS activation. However, the neutralization between bonded N and B atoms (B

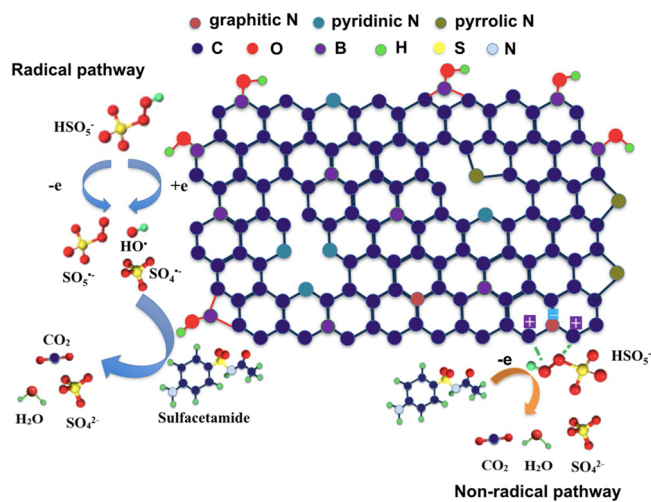


Fig. 10. Mechanism of PMS activation and SAM degradation on 2sNBG800.

ortho to N, B-N bond) results in the poorer performance of SAM degradation by 1sNBG (h-BN/NBG hybrid)/PMS. The proposed catalytic mechanism on different sites of 2sNBG800 for PMS activation is illustrated in Fig. 10.

3.4. Proposed major SAM degradation pathway and ecotoxicity of products

The transformation products (TPs) in the 2sNBG800/PMS/SAM system were analyzed by LC-MS/MS. Based on the seven TPs identified in the mass spectra (Fig. S8), the three possible pathways for SAM degradation pathway are profiled in Fig. 11. In the first SAM degradation pathway, the amine group connected with benzene ring can be oxidized to nitroso and nitro groups by ROS to form the TP A (m/z (-) 227.1) and TP B (m/z (-) 243.1), respectively. Then cleavage of the S-C bond in the nitro-substitutional SAM (TP B) can be induced to form NB (TP C, m/z (-) 122.0). NB can be hydroxylated into TP D (m/z (-) 138.1) before mineralization via ring opening. The second SAM degradation pathway can be initiated by direct removal of the amine group on the benzene ring of SAM to generate the TP E (m/z (-) 198.1). In the third SAM degradation pathway, the nitroso-substitutional SAM (TP A) can be polymerized with another benzene ring to produce TP F (m/z (-) 303.1). Another polymerized TP G (m/z (-) 477.2) has also been detected. Afterwards, the TPs can proceed to be degraded via ring opening and formation of small molecular derivatives (e.g. alcohols and acids), and

finally be mineralized into SO_4^{2-} , NO_3^- , CO_3^{2-} , CO_2 and H_2O .

To evaluate the ecotoxicity of SAM and its TPs, the influences of SAM and its TPs on various species (e.g., fish, daphnid and green algae) were estimated using QSAR analysis via ECOSAR program. Generally, three main types of TPs were generated in the 2sNBG800/PMS/SAM system: 1) nitroso- and nitro- derivatives, which can relate to the inclination of SO_4^{2-} to attack -NH₂ group; 2) hydroxylated products, which can relate to the reaction between SAM and HO[·]; and 3) dimeric products, which can relate to the recombination of N-centered radicals caused by SO_4^{2-} [63,64]. TPs showed different acute toxicity levels (predicted by Half Effective Concentration (EC₅₀) or Half Lethal Concentration (LC₅₀)) for different species, in which, green algae are the most sensitive species. With respect to the chronic toxicity (predicted by Chronic Value (ChV)), fish is the most sensitive species. All the TPs demonstrated a lower EC₅₀ or LC₅₀ value than that of SAM (Table S3), indicating that TPs have a higher acute toxicity than SAM. Similarly, the chronic toxicities of all the TPs are higher than that of SAM except for TP C (Table S3). Despite the increase in toxicity after initial degradation, significant mineralization also occurred in the 2sNBG800/PMS/SAM system, which can be observed from the 84% TOC removal efficiency (reaction time = 60 min). (Fig. S9). From the results, it can be concluded that the transformation of amine groups and subsequent mineralization can effectively reduce the harmful effect of sulfonamides to the environment. 2sNBG fabricated by the two-step synthesis method in this study is effective in mineralizing the recalcitrant pollutant via PMS activation.

3.5. Practical application

3.5.1. Effect of common matrix species

The actual wastewater usually contains inorganic ions (e.g., Cl^- , SO_4^{2-} , Mg^{2+} , and Na^+ , etc.) and organics. Especially, humic acid (soluble in alkaline media and insoluble at pH 1) is the principal component of humic substances which account for 50–80% of dissolved organic carbon (DOC) in natural waters with respect to dissolved organic carbon [65,66]. Some of the common aqueous matrix species serve as the quenching agents to diminish the catalytic performance in the 2sNBG800/PMS/SAM system. Background matters such as Cl^- , NO_3^- and humic acid were selected in this study and their concentrations were set according to the real secondary wastewater effluent [67]. As shown in Fig. 12, NO_3^- exerted a negligible influence (< 5% reduction in k_{app}) on the PMS activation by 2sNBG800 to degrade SAM. Cl^- exhibited an adverse impact on the catalytic oxidation of SAM (33% reduction in k_{app}), which is associated with the high second order reaction

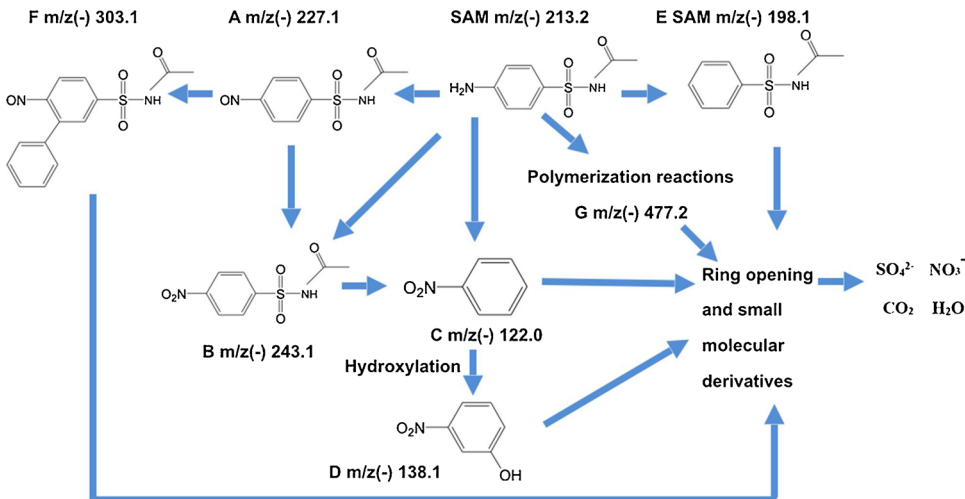


Fig. 11. The main SAM degradation pathways in the 2sNBG800/PMS/SAM system (Condition: [PMS] = 0.5 mM, [SAM] = 10 mg L⁻¹, [catalyst] = 0.2 g L⁻¹, pH = 7).

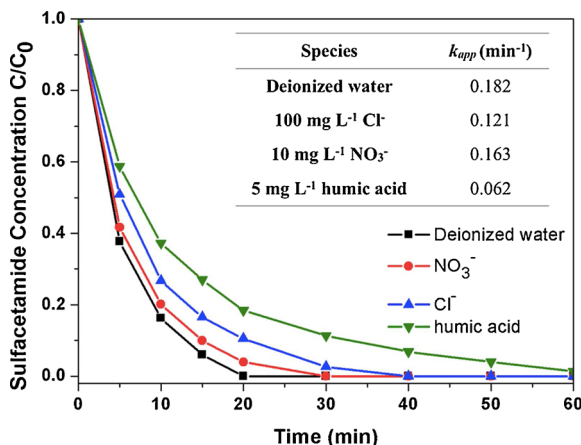


Fig. 12. The effect of common matrix species on the SAM degradation by 2sNBG800/PMS (Condition: [PMS] = 0.5 mM, [SAM] = 10 mg L⁻¹, [catalyst] = 0.2 g L⁻¹, [Cl⁻] = 100 mg L⁻¹, [NO₃⁻] = 10 mg L⁻¹, [humic acid] = 5 mg L⁻¹, pH = 7).

rate constant between Cl⁻ and SO₄²⁻ in the 2sNBG800/PMS/SAM system ($k_{SO_4^{2-}+Cl^-} = 2.0 \times 10^8 \text{ M}^{-1} \text{ s}^{-1}$) [68]. Humic acid suppressed the SAM degradation most (64% decrease in k_{app}). This suppression can be attributed to the competition for ROS between SAM and humic acid (comprising organics with carbon and oxygen-based moieties, such as carboxylate, carbonyl and phenolic groups with high reactivity [69]) in the 2sNBG800/PMS/SAM system.

3.5.2. Reusability

Fig. 13(a) demonstrates the stability of 2sNBG800. In comparison to 100% SAM removal within 20 min (0.182 min⁻¹) by the fresh 2sNBG800 in the 1st run, to achieve 100% SAM removal entailed 40 and 60 min in the 2nd (0.093 min⁻¹) and 3rd run (0.061 min⁻¹), respectively (Table S2). The chemical composition of the 2sNBG800 3rd run (2sNBG800 used after 3 consecutive cycles) was analyzed by XPS (Tables 5a and 5b and Fig. S10). Compared with the fresh 2sNBG800, the N/C ratio of 2sNBG800 3rd run showed negligible change albeit with 41% and 22% declines in B/C and O/C ratios, respectively (Table 5a). The reduction of B/C and O/C ratios mainly correspond to the leaching of B element from B₂O₃ (Table S2). Meanwhile, the content of pyridinic N and BC3 in 2sNBG800 3rd run demonstrated an insignificant change (< 10% reduction) in comparison to that of the fresh 2sNBG800 (Table 5b), suggesting that the catalytic sites are considerably stable for PMS activation.

FTIR analysis was conducted for 2sNBG800 3rd run. As shown in Fig. 13(b), the intensities of the peaks centered at ~1350 cm⁻¹ and ~3400 cm⁻¹ increased, which is associated with the adsorption of SAM degradation intermediates. It has been reported that the asymmetric stretch of S=O bond in sulfonamides is at 1325 cm⁻¹, the symmetric stretch of the aromatic nitro group is at 1355–1315 cm⁻¹, and NH₂ stretch in sulfonamides is at 3350–3250 cm⁻¹ [70]. In addition, the rapid weight loss can be observed in the TGA curve of the 2sNBG800 3rd run (Fig. 13(c)), which suggests the existence of the adsorbed intermediates and corresponds to the FTIR result. Thus, the main reason for the deactivation of 2sNBG800 is that the adsorbed intermediates occupied the active sites on the 2sNBG800 surface. Thermal regeneration (annealing at 350 °C under nitrogen atmosphere for 2 h with the heating rate of 5 °C min⁻¹) was applied to burn the adsorbed intermediates covering the active sites of 2sNBG800 3rd run. The catalytic activity was recovered with 100% removal of SAM within 30 min ($k_{app} = 0.102 \text{ min}^{-1}$) compared with 2sNBG800 3rd run (100% removal of SAM within 60 min, $k_{app} = 0.061 \text{ min}^{-1}$) (Fig. S11). Further effort can be put into developing more robust carbocatalysts engineered with desirable functionalities which can improve the surface affinity,

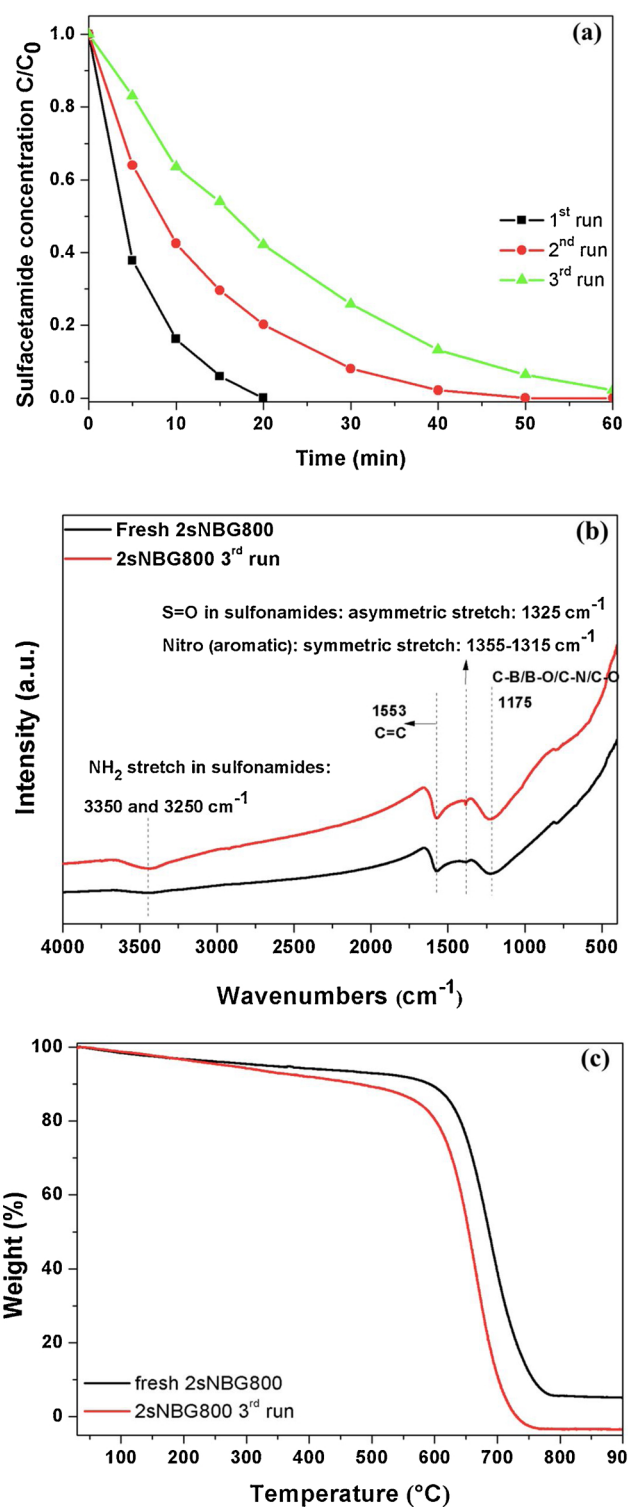


Fig. 13. (a) Reusability of 2sNBG800 (Condition: [PMS] = 0.5 mM, [SAM] = 10 mg L⁻¹, [catalyst] = 0.2 g L⁻¹, pH = 7). FTIR spectrum (b) and TGA curve (c) of the 2sNBG800 3rd run.

Table 5a
Chemical composition of the fresh 2sNBG800 and used 2sNBG800.

	C at.%	O at.%	N at.%	B at.%	O/C	N/C	B/C	N/B
Fresh 2sNBG800	56.6	13.2	13.8	16.3	0.23	0.24	0.29	0.84
2sNBG800 3 rd run	64.5	11.7	12.3	11.2	0.18	0.19	0.17	1.09

Atomic percentages of C, O, N and B were analyzed by XPS.

Table 5bXPS deconvolution information of the fresh 2sNBG800 and 2sNBG800 3rd run.

	pyridinic N N _{pyridinic-N} /N _{total} (%)	pyrrolic N N _{pyrrolic-N} /N _{total} (%)	graphitic N N _{graphitic-N} /N _{total} (%)	BC3 B _{BC3} /B _{total} (%)	BC2O/BCO2 B _{BC2O} or BCO2/B _{total} (%)
Fresh 2sNBG800	73.4	23.2	3.4	42.4	56.6 (BC2O)
2sNBG800 3 rd run	66.0	26.4	7.6	41.0	59.0 (BC2O)

Atomic percentages of pyridinic N, pyrrolic N, graphitic N, BC3 and BC2O/BCO2 were analyzed by XPS.

complexity and electrostatic charge of carbocatalyst and therefore facilitate surface-based non-radical pathway, so as to alleviate radical quenching effects of the background organic and inorganic matters.

4. Conclusion

In summary, this study carried out a two-step thermal annealing approach to produce 2sNBG without h-BN. The concentration of N and B dopants and the content of pyridinic N and BC3 of 2sNBGs showed a similar trend with elevated T_a (increasing from 600 to 800 °C and decreasing at 900 °C). 2sNBG800 exhibited the best catalytic activity for PMS activation to degrade SAM. In contrast, the one-step thermal annealing would lead to the formation of a h-BN/NBG hybrid (1sNBG). The elevated T_a induced an insignificant difference in the catalytic activity of 1sNBGs. Two-step thermal annealing was superior in generating an ideal PMS activator for SAM degradation over one-step thermal annealing. The catalytic performance of the doped carbocatalysts followed the order of 2sNBG800 > 2sNBG900 > 2sNBG700 > 2sNBG600 > NG600 > 1sNBGs > BG800. Both experimental results and DFT calculation collectively unveiled the mechanism for the remarkable catalytic efficiency of 2sNBG800. The reasons can be described as below: 1) both radical and non-radical oxidative reaction existed in the 2sNBG/PMS system, while NG/PMS was a non-radical-dominated system; and 2) the synergistic coupling effect between pyridinic N and BC3 (B-C-C-pyridinic N) brought in more positively charged carbon atoms as active sites for PMS activation. The neutralization effect in the B–N bond resulted in the poor performance of SAM degradation by 1sNBG (h-BN/NBG hybrid)/PMS. The transformation of the amine group and subsequent mineralization can effectively reduce the hazardous effect of sulfonamides to the environment. The presence of Cl⁻ and humic acid can adversely affected the SAM removal in 2sNBG/PMS system. The occupation of active sites on the surface of 2sNBG by the adsorbed intermediates was the major reason for the deactivation of 2sNBG. Further efforts can be carried out to investigate the role of synthesis parameters in formation of N–B bonding configurations and develop more robust carbocatalysts engineered with rational functionalities toward practical application. This study contributes to a deeper insight into the functions of different N–B bonding configurations in carbocatalysis for PMS activation and provides an advanced strategy for fabricating green and high-performance carbocatalysts in environmental remediation.

Acknowledgement

This research is supported by Ministry of Education, Singapore, under the Academic Research Grant RG96/16. X. D. appreciate the partial support from Open Research Projects of State Key Laboratory (SKL-ChE-16C05 and QAK201808).

Appendix A. Supplementary data

Supplementary material related to this article can be found, in the online version, at doi:<https://doi.org/10.1016/j.apcatb.2019.04.018>.

References

- [1] W.D. Oh, Z. Dong, T.T. Lim, Appl. Catal. B Environ. 194 (2016) 169–201.
- [2] P. Hu, M. Long, Appl. Catal. B Environ. 181 (2016) 103–117.
- [3] X. Duan, H. Sun, S. Wang, Acc. Chem. Res. (2018).
- [4] K.-Y.A. Lin, Z.-Y. Zhang, Chem. Eng. J. 313 (2017) 1320–1327.
- [5] J. Chen, W. Hong, T. Huang, L. Zhang, W. Li, Y. Wang, Environ. Sci. Pollut. Res. 23 (2016) 18564–18574.
- [6] Y. Wang, J.B. Chen, T.Y. Huang, C.Y. Wei, Desalin. Water Treat. 71 (2017) 159–167.
- [7] H. Wang, T. Maiyalagan, X. Wang, ACS Catal. 2 (2012) 781–794.
- [8] A.K. Geim, K.S. Novoselov, Nat. Mater. 6 (2007) 183–191.
- [9] K.S. Novoselov, V.I. Fal'ko, L. Colombo, P.R. Gellert, M.G. Schwab, K. Kim, Nature 490 (2012) 192–200.
- [10] X. Chen, W.D. Oh, T.T. Lim, Chem. Eng. J. 354 (2018) 941–976.
- [11] W.-D. Oh, G. Lisak, R.D. Webster, Y.-N. Liang, A. Veksha, A. Giannis, J.G.S. Moo, J.-W. Lim, T.-T. Lim, Appl. Catal. B Environ. 233 (2018) 120–129.
- [12] X. Chen, W.D. Oh, Z.T. Hu, Y.M. Sun, R.D. Webster, S.Z. Li, T.T. Lim, Appl. Catal. B Environ. 225 (2018) 243–257.
- [13] X. Duan, Z. Ao, H. Sun, S. Indrawirawan, Y. Wang, J. Kang, F. Liang, Z.H. Zhu, S. Wang, ACS Appl. Mater. Interfaces 7 (2015) 4169–4178.
- [14] D. Li, X. Duan, H. Sun, J. Kang, H. Zhang, M.O. Tade, S. Wang, Carbon 115 (2017) 649–658.
- [15] H. Chen, K.C. Carroll, Environ. Pollut. 215 (2016) 96–102.
- [16] X. Wang, Y. Qin, L. Zhu, H. Tang, Environ. Sci. Technol. 49 (2015) 6855–6864.
- [17] P. Liang, C. Zhang, X. Duan, H. Sun, S. Liu, M.O. Tade, S. Wang, Environ. Sci. Nano 4 (2017) 315–324.
- [18] X. Duan, S. Indrawirawan, H. Sun, S. Wang, Catal. Today 249 (2015) 184–191.
- [19] X. Duan, K. O'Donnell, H. Sun, Y. Wang, S. Wang, Small 11 (2015) 3036–3044.
- [20] H. Sun, Y. Wang, S. Liu, L. Ge, L. Wang, Z. Zhu, S. Wang, Chem. Commun. 49 (2013) 9914–9916.
- [21] W. Ma, N. Wang, Y. Du, P. Xu, B. Sun, L. Zhang, K.-Y.A. Lin, ACS Sustain. Chem. Eng. 7 (2019) 2718–2727.
- [22] D. Jana, C.L. Sun, L.C. Chen, K.H. Chen, Prog. Mater. Sci. 58 (2013) 565–635.
- [23] J. Tai, J. Hu, Z. Chen, H. Lu, RSC Adv. 4 (2014) 61437–61443.
- [24] S. Wang, L. Zhang, Z. Xia, A. Roy, D.W. Chang, J.B. Baek, L. Dai, Angew. Chem. Int. Ed. 51 (2012) 4209–4212.
- [25] Y. Zheng, Y. Jiao, L. Ge, M. Jaroniec, S.Z. Qiao, Angew. Chem. Int. Ed. 52 (2013) 3110–3116.
- [26] F. Yang, Y. Cao, Z. Chen, X. He, L. Hou, Y. Li, New J. Chem. 42 (2018) 2718–2725.
- [27] W. Lei, D. Portehault, D. Liu, S. Qin, Y. Chen, Nat. Commun. 4 (2013) 1777.
- [28] S. Jia, Z. Wang, N. Ding, Y.L. Elaine Wong, X. Chen, G. Qiu, T.W. Dominic Chan, Anal. Chim. Acta 936 (2016) 123–129.
- [29] H. Tabassum, R. Zou, A. Mahmood, Z. Liang, S. Guo, J. Mater. Chem. A 4 (2016) 16469–16475.
- [30] C. Yu, H. Fang, Z. Liu, H. Hu, X. Meng, J. Qiu, Nano Energy 25 (2016) 184–192.
- [31] J. Chen, X. Zhou, Y. Zhang, H. Gao, Sci. Total Environ. 432 (2012) 269–274.
- [32] Q. Zhang, A. Jia, Y. Wan, H. Liu, K. Wang, H. Peng, Z. Dong, J. Hu, Environ. Sci. Technol. 48 (2014) 14317–14325.
- [33] W.-D. Oh, V.W.C. Chang, Z.-T. Hu, R. Goei, T.-T. Lim, Chem. Eng. J. 323 (2017) 260–269.
- [34] Y. Bao, W.-D. Oh, T.-T. Lim, R. Wang, R.D. Webster, X. Hu, Water Res. 151 (2019) 64–74.
- [35] W.S. Hummers Jr, R.E. Offeman, J. Am. Chem. Soc. 80 (1958) 1339.
- [36] B. Yuan, W. Xing, Y. Hu, X. Mu, J. Wang, Q. Tai, G. Li, L. Liu, K.M. Liew, Y. Hu, Carbon 101 (2016) 152–158.
- [37] S. Wakeland, R. Martinez, J.K. Grey, C.C. Luhrs, Carbon 48 (2010) 3463–3470.
- [38] S. Stankovich, D.A. Dikin, R.D. Piner, K.A. Kohlhaas, A. Kleinhammes, Y. Jia, Y. Wu, S.T. Nguyen, R.S. Ruoff, Carbon 45 (2007) 1558–1565.
- [39] Z. Lin, G. Waller, Y. Liu, M. Liu, C.P. Wong, Adv. Energy Mater. 2 (2012) 884–888.
- [40] D. Lee, B. Lee, K.H. Park, H.J. Ryu, S. Jeon, S.H. Hong, Nano Lett. 15 (2015) 1238–1244.
- [41] X. Xu, T. Yuan, Y. Zhou, Y. Li, J. Lu, X. Tian, D. Wang, J. Wang, Int. J. Hydrogen Energy 39 (2014) 16043–16052.
- [42] S.M. Jung, E.K. Lee, M. Choi, D. Shin, I.Y. Jeon, J.M. Seo, H.Y. Jeong, N. Park, J.H. Oh, J.B. Baek, Angew. Chem. Int. Ed. 53 (2014) 2398–2401.
- [43] P. Serp, B. Machado, Nanostructured Carbon Materials for Catalysis, Royal Society of Chemistry, Cambridge, UK, 2015.
- [44] L.E. Jones, P.A. Thrower, J. Chim. Phys. Phys. Chim. Biol. 84 (1987) 1431–1438.
- [45] D.W. McKee, Chem. Phys. Carbon 23 (1991) 173–232.
- [46] Y.J. Lee, L.R. Radovic, Carbon 41 (2003) 1987–1997.
- [47] T.W. Lin, C.Y. Su, X.Q. Zhang, W.J. Zhang, Y.H. Lee, C.W. Chu, H.Y. Lin, M.T. Chang, F.R. Chen, L.J. Li, Small 8 (2012) 1384–1391.

- [48] S.K. Young, J. Park, C.C. Hyun, P.A. Jae, Q.H. Jin, S.K. Hong, *J. Am. Chem. Soc.* 129 (2007) 1705–1716.
- [49] Y. Zhao, L. Yang, S. Chen, X. Wang, Y. Ma, Q. Wu, Y. Jiang, W. Qian, Z. Hu, *J. Am. Chem. Soc.* 135 (2013) 1201–1204.
- [50] X. Chen, Q. Qiao, L. An, D. Xia, *J. Phys. Chem. C* 119 (2015) 11493–11498.
- [51] L. Qu, Y. Liu, J.B. Baek, L. Dai, *ACS Nano* 4 (2010) 1321–1326.
- [52] G.R. Bhimanapati, D. Kozuch, J.A. Robinson, *Nanoscale* 6 (2014) 11671–11675.
- [53] X.-k. Ma, N.-H. Lee, H.-J. Oh, S.-C. Jung, W.-J. Lee, S.-J. Kim, *J. Cryst. Growth* 316 (2011) 185–190.
- [54] W.-D. Oh, M.G.H. Lee, W.D. Chanaka Udayanga, A. Veksha, Y. Bao, A. Giannis, J.-W. Lim, G. Lisak, *J. Environ. Chem. Eng.* 7 (2019) 102872.
- [55] X. Blase, J.C. Charlier, A. De Vita, R. Car, *Appl. Phys. a-Mater.* 68 (1999) 293–300.
- [56] D. Golberg, P. Dorozhkin, Y. Bando, M. Hasegawa, Z.C. Dong, *Chem. Phys. Lett.* 359 (2002) 220–228.
- [57] D. Golberg, Y. Bando, P. Dorozhkin, Z.C. Dong, *MRS Bull.* 29 (2004) 38–42.
- [58] X. Wu, L.R. Radovic, *Carbon* 43 (2005) 1768–1777.
- [59] X. Duan, H. Sun, Z. Ao, L. Zhou, G. Wang, S. Wang, *Carbon* 107 (2016) 371–378.
- [60] E.T. Yun, J.H. Lee, J. Kim, H.D. Park, J. Lee, *Environ. Sci. Technol.* 52 (2018) 7032–7042.
- [61] J. Chen, L. Zhang, T. Huang, W. Li, Y. Wang, Z. Wang, *J. Hazard. Mater.* 320 (2016) 571–580.
- [62] F. Ghanbari, M. Moradi, *Chem. Eng. J.* 310 (Part 1) (2017) 41–62.
- [63] Y. Yang, X.L. Lu, J. Jiang, J. Ma, G.Q. Liu, Y. Cao, W.L. Liu, J. Li, S.Y. Pang, X.J. Kong, C.W. Luo, *Water Res.* 118 (2017) 196–207.
- [64] S. Luo, Z. Wei, D.D. Dionysiou, R. Spinney, W.-P. Hu, L. Chai, Z. Yang, T. Ye, R. Xiao, *Chem. Eng. J.* 327 (2017) 1056–1065.
- [65] N. Hertkorn, H. Claus, P. Schmitt-Kopplin, E.M. Perdue, Z. Filip, *Environ. Sci. Technol.* 36 (2002) 4334–4345.
- [66] P. Janoš, *J. Chromatogr. A* 983 (2003) 1–18.
- [67] W.-D. Oh, S.-K. Lua, Z. Dong, T.-T. Lim, *J. Hazard. Mater.* 284 (2015) 1–9.
- [68] J.L. Redpath, R.L. Willson, *Int. J. Radiat. Biol.* 27 (1975) 389–398.
- [69] Y.C. Bai, F.C. Wu, C.Q. Liu, W. Li, J.Y. Guo, P.Q. Fu, B.S. Xing, J. Zheng, *Anal. Chim. Acta* 616 (2008) 115–121.
- [70] D.L. Pavia, G.M. Lampman, G.S. Kriz, J.R. Vyvyan, *Introduction to Spectroscopy*, fifth ed., Cengage Learning, Stamford, CT, 2015.